Pt NP-MWCNT Composite Electrodes with a Reduced Pt Loading for the Hydrogen Evolution Reaction

by

Remi Laraque

Supervised by

Sylvain Coulombe

Sasha Omanovic

Submitted as partial requirement for the

Master's Degree in Chemical Engineering

at

McGill University

Montréal, Québec,

April 4th, 2016

Table of Content

List of Figures iv
List of Table vi
Abstract vii
Abrégé ix
Acknowledgments xi
Symbols and Abbreviation xii
1 Introduction 1
1.1 Context 1
1.2 Rationale and Objective 2
2 Background and Theory 4
2.1 Electrocatalysis 4
2.1.1 The Double Layer 4
2.1.2 Potential in the Electrolytic Cell 5
2.1.3 Current and Reaction Rate 6
2.1.4 Kinetics 8
2.2 Hydrogen Evolution Reaction (HER) in Electrocatalysis 11
2.2.1 Mechanism of HER 11
2.2.2 Metal Catalysts for the HER 13
2.3 Carbon Nanotubes 14
2.3.1 Electronic Structure 15
2.3.2 CNT Properties 16
2.3.3 Fundamentals of CNT Synthesis 18
2.4 Laser Ablation 22
2.4.1 Laser Fundamentals 22
2.4.2 Laser Operation 24
2.4.3 Nanoparticle Production 25
3 Experimental Methods 26
3.1 Electrode Fabrication 26
3.1.1 Carbon Nanotubes 26

3.1.2 Platinum Nanoparticles 28
3.2 Electrochemical Testing Cell 31
3.3 Characterization Techniques 32
3.3.1 Electron Microscopy 32
3.3.2 Linear Tafel Polarization 33
3.3.3 Chronopotentiometry 33
4 Results and Discussion 35
4.1 Physical Characterization 35
4.1.1 Electrode Morphology 35
4.1.2 Morphology of Platinum on MWCNT 38
4.1.3 Particle Size Distribution 42
4.2 Electrochemical Characterization 45
4.2.1 Tafel Plot in Acidic Conditions 45
4.2.2 Tafel Plot in Alkaline Conditions 52
4.2.3 Electrode Stability 57
4.3 Comparison of Electrode Performance with Literature 60
5 Conclusion 61
6 References 63

List of Figures

Figure 2.1-A schematic illustration of the electrical double layer and potential distribution near an electrode surface. 5

Figure 2.2- Processes involved in electrode reactions 7

Figure 2.3- Exchange current densities for the HER versus work functions of metals: (a) refers to transition metals and sp metals with positively charged surfaces and (b) refers to sp metals with negatively charged surfaces 13

Figure 2.4-Exchange current densities for the HER vs. strength of M-H bond..... 14

Figure 2.5-Schematic of a 2D graphene sheet illustrating lattice vectors $\mathbf{a_1}$ and $\mathbf{a_2}$ and the roll up vector $\mathbf{C_h} = n\mathbf{a_1} + m\mathbf{a_2}$. The limiting, achiral cases of (n,0) zigzag and (n, n) armchair are indicated with dashed lines. The translation vector **T** lies along the nanotube axis and defines the 1D unit cell. The shaded, boxed area represents the unrolled unit cell formed by **T** and $\mathbf{C_h}$. The diagram is constructed for (n, m) = (4,2) [21]. 16

Figure 2.6-A) A conceptual diagram of i) SWCNT and ii) MWCNT showing typical dimensions of length, width, and separation distance between graphene layers in MWCNTs. B) TEM micrographs: i) MWCNT, and with magnification in ii) structure [22] 17

Figure 2.7-Schematic of tip-growth and extrusion mechanisms for carbon filament growth via CVD 21

Figure 2.8-Scheme of a two-level system illustrating: a) stimulated absorption, b) spontaneous emission, and c) stimulated emission phenomena. 23

Figure 2.9-Schematic of Nd-YAG laser 25

Figure 3.1-Schematic of thermal chemical vapor deposition setup 28

Figure 3.2- Schematic of laser ablation setup (not to scale) 30

Figure 3.3-Photograph of laser ablation setup 30

Figure 3.4-Schematic of a three-electrode electrochemical cell used for characterization on composite electrodes 32

Figure 4.1-Morphology of the electrode along the production process. A) Bare stainless steel mesh. B) Mesh covered with Pt NP-MWCNTs. C) Bare MWCNTs. D) MWCNT covered with Pt nanoparticles 36

Figure 4.2-EDS analysis of: A) MWCNT after 10 min of PLA; B) Bare MWCNT 38

Figure 4.3-TEM images showing the morphology of PLA deposited platinum on MWCNTs. A. Deposition time of 2.5 minutes; B. Deposition time of 10 minutes; C. Deposition time of 20 minutes; D. Deposition time of 40 minutes 40

Figure 4.4-Dark field TEM images showing the morphology of PLA deposited platinum nanoparticles on MWCNTs. A. Deposition time of 2.5 min; B. Deposition time of 10 min; C. Deposition time of 20 min; D. Deposition time of 40 min 41

Figure 4.5-Platinum nanoparticle size distribution with a deposition time of 2.5 minutes 42

Figure 4.6-Platinum nanoparticle size distribution with a deposition time of 10 minutes 43

Figure 4.7-Surface mass density of platinum nanoparticles deposited as a function of ablation time 44

Figure 4.8-Tafel plot: Current density as a function of overpotential for various electrodes in 0.5 M H2SO4. (a) Platinum wire, (b) Bare MWCNT, (c) 2 min 30s Pt NP-MWCNT, (d) 5 min Pt NP-MWCNT, (e) 10 min Pt NP-MWCNT, (f) 20 min Pt NP-MWCNT, (g) 30 min Pt NP-MWCNT. 47

Figure 4.9- Current density of various composite electrodes as a function of PLA time (measured in 0.5M H2SO4)..... 49

Figure 4.10-Current density normalized by mass of various composite electrodes as a function of PLA time (measured in 0.5M H_2SO_4)..... 50

Figure 4.11-Tafel plot: Current density as a function of overpotential for various electrodes in 0.1M NaOH (a) Platinum wire, (b) Bare MWCNT, (c)2 min 30s Pt NP-MWCNT, (d) 5 min Pt

NP-MWCNT, (e) 10 min Pt NP-MWCNT, (f) 20 min Pt NP-MWCNT, (g) 30 min Pt NP-MWCNT. 52

Figure 4.12- Current density of various composite electrodes as a function of PLA time (measured in 0.1M NaOH) 54

Figure 4.13- Current density normalized by mass of various composite electrodes as a function of PLA time (measured in 0.1M NaOH)..... 55

Figure 4.14-Measured potential versus time for an applied current density of 200 mA.cm^{-2} in 1M NaOH (the same electrode is used in both cycles). A) First cycle B) Second Cycle 58

Figure 4.15-Comparison of the average measured potential versus time for an applied current density of 200 mA.cm-2 in 1M NaOH (the same electrode is used in both cycles)..... 59

List of Table

Table 1- Tafel parameters of Pt NP-MWCNT composite electrodes for various PLA times in acid electrolyte. (Presented Error is standard deviation from the mean)..... 51

Table 2-Tafel parameters of Pt NP-MWCNT composite electrodes for various PLA times in basic electrolyte. (Presented Error is standard deviation from the mean)..... 56

Abstract

This Master's thesis presents the investigation of a novel electrode for use in the electrolysis of water in acidic or alkaline conditions with the aim of producing hydrogen gas. The core structure of the electrode is composed of multiwall carbon nanotubes (MWCNT) due to their high surface area and electrical conductivity. Also this material has been shown to be stable in electrochemical operations [1]. Platinum nanoparticles were deposited on the nanotubes. This metal was chosen since it has been extensively studied and is known to be the best catalyst for the hydrogen evolution reaction [2]. Since platinum is a very expensive material, its loading on the electrode must be minimized, which was the goal of the work.

The MWCNTs were produced using chemical vapor deposition technique developed by Baddour et al.[3] which enable the growth of CNT directly on a stainless steel substrate for an optimal electrical conductivity. Platinum nanoparticles were synthesized using a pulsed laser ablation method. The electrodes were characterized using high-resolution electron microscopy (SEM and TEM). The study of the electrocatalytic activity of the electrode was done using linear Tafel polarization (LTP). Chronopotentiometry was used to assess the stability of the electrode.

The MWCNTs produced formed a dense three dimensional network with high surface area per unit volume. The Pt nanoparticles produced homogeneously dispersed and stable particles. The particle sizes followed a lognormal distribution with an average particle size of 3.6 nm. The composite electrode had a reduced Pt loading ranging from 0.03 to 0.2 $mg.cm^{-2}$ as opposed to commercial electrolyzer catalysts which have loadings ranging from 1 to 4 $mg.cm^{-2}$. The electrochemical activity of the electrodes was tested in 1M NaOH at atmospheric pressure and temperature. At an overpotential η=110 mV the lowest loading electrode (0.04 $mg.cm^{-2}$) had a current density of 10.3 $mA.cm^{-2}$. The higher loading electrode (0.2 $mg.cm^{-2}$) had a current density of 89.9 $mA.cm^{-2}$. In acidic conditions measurements were done in 0.5M H_2SO_4 at an overpotential of 90 mV. At the low loading of 0.03 $mg.cm^{-2}$ a current density of 53 $mA.cm^{-2}$ was recorded, while a current density of 340 $mA.cm^{-2}$ was obtained for a Pt loading of 0.2 $mg.cm^{-2}$. The stability test showed that the platinum particles were stable on the MWCNTs. However, the intense hydrogen

bubbling from the surface causes some blockage on the surface which slightly reduced the performance of the electrode.

Abrégé

Cette thèse de maîtrise présente une étude sur l'utilisation d'une nouvelle électrode pour la production d'hydrogène via l'électrolyse de l'eau en milieu acide et alcalin. Cette électrode est formée de nanotubes de carbone à parois multiples (NTCPMs) en raison de leur large surface et bonne conductivité. De plus, des études précédentes utilisant ce matériau ont démontré sa stabilité dans des milieux électrochimiques corrosifs[1]. Des nanoparticules de platine ont été déposé sur les nanotubes. Ce métal a été choisi car ses propriétés catalytiques ont été étudié en profondeur par le passé. Par ailleurs, il a été prouvé que ce matériau est le meilleur catalyseur pour la réduction d'hydrogène atomique en hydrogène moléculaire[2]. Le platine étant un matériau très dispendieux, il est essentiel de limité la masse utilisée au strict minimum pour un niveau de performance donné.

Les nanotubes ont été produits par une méthode de dépôt chimique en phase gazeuse développée par Baddour et al.[3]. Cette technique permet la croissance des nanotubes directement à partir d'un maillage d'acier inoxydable formant ainsi une connexion électrique optimale entre le maillage et les nanotubes. Quant aux nanoparticules de platine, elles ont été produites par ablation laser pulsé. Les électrodes ont été caractérisés par microscopie électronique à haute résolution. L'activité catalytique des électrodes a été déterminée par voltammétrie à balayage linéaire. La stabilité des particules de platine a été étudiée par cyclage galvanostatique.

Les nanotubes produits forment un réseau dense et poreux avec une très grande surface par unité de volume. De plus, les résultats obtenus démontrent que les particules de platine produites sont dispersées de manière homogène et solidement ancrées sur les nanotubes. La taille des particules est distribuée de manière log normale avec une taille moyenne de 3.4 nm. La masse par unité de surface des nanoparticules de platine sur ces électrodes est de 0.03 à 0.20 $mg.cm^{-2}$. L'activité électrochimique des électrodes a été testé dans une solution de NaOH. A un surpotentiel de η=110 mV, l'électrode avec la plus faible masse de platine (0.04 $mg.cm^{-2}$) indique une densité de courant de 10.3 $mA.cm^{-2}$. L électrode avec la masse la plus élevé (0.2 $mg.cm^{-2}$) démontre une densité de courant de 89.9 $mA.cm^{-2}$. Dans des conditions acides les mesures ont été faites dans une solution de 0.5M H_2SO_4 à un surpotentiel de 90 mV. Avec une faible masse de platine de 0.03

$mg.cm^{-2}$, une densité de courant de 53 $mA.cm^{-2}$ est obtenu alors qu'une densité de courant de 340 $mA.cm^{-2}$ est observée pour une masse de 0.2 $mg.cm^{-2}$. Les tests de stabilité ont démontré que les particules de platine sont ancrées de manière stable sur les nanotubes de carbone. Cependant, la production vigoureuse d'hydrogène moléculaire à la surface des électrodes cause un certain blocage de la surface ce qui cause une réduction de performance.

Acknowledgments

I would first like to thank my research supervisors, professors Sylvain Coulombe and Sasha Omanovic for their support and wisdom throughout my journey in graduate school. I have been amazingly fortunate to have research supervisors that gave me the freedom to explore on my own, and at the same time the guidance to recover when my steps faltered. Finally, your straightforward and friendly attitude has truly made the experience a positive one.

Next, I would like to thank my family, particularly my parents for their love and continued support throughout not only my graduate career but also my undergrad. Without your support I would not have been through this adventure at McGill University in the great city of Montreal.

I would like to thank my colleagues from the Plasma Processing Laboratory and the Electrochemistry and Corrosion Laboratory.

I would also like to give a special thanks to Mathew, Pablo, Pierre, Ulrich and Mahmoud for making my time as graduate student an incredibly pleasant one.

Nathan, I want to thank you for pointing me in the right direction when my project reached a great road block. Without your input I would probably still be in the lab instead of wrapping up my thesis.

To my colleague Dr. Mark McArthur I want to give a great deal of thanks for countless advice, direction, training along my project. I want to thank you for your pioneering role in our research groups which allowed my project to flow smoothly. Finally, I want to thank you for being a great desk mate and a great lifting buddy.

Symbols and Abbreviation

A	Active surface area, cm^{-2}
$\mathbf{C}_h$	Orthogonal vector
CE	Counter electrode
CNT	Carbon nanotubes
EDL	Electric double layer
EDX	Energy-Dispersive X-Ray Spectroscopy
GS	Graphene sheet
HER	Hydrogen evolution reaction
H_2SO_4	Sulfuric acid
I	Current, A
IHL/OHL	Inner/outer Helmholtz Layer
j	Current density, $A.cm^{-2}$
LTP	Linear Tafel polarization
MWCNT	Multi-walled carbon nanotubes
NaOH	Sodium hydroxide
PLA	Pulsed laser ablation
PPL	Plasma Processing Laboratory
RE	Reference electrode
RDS	Rate determining step
SCE	Saturated calomel electrode
SEM	Scanning electron microscopy
SHE	Standard hydrogen electrode
SWCNTs	Single-walled carbon nanotubes
t	Time, s
t-CVD	Thermal Chemical Vapor Deposition
T	Translational vector

TEM	Transmission electron microscopy
WE	Working electrode
Φ	Metal work function

1 Introduction

1.1 Context

Satisfying the ever-increasing demand in energy is one of the great challenges of the 21st century. The growing atmospheric concentration of carbon dioxide is a direct consequence of the use of fossil fuels. CO_2 is the most abundant by-product of the combustion of fossil fuels. This very stable compound is recognized as a major contributor to the greenhouse effect. Furthermore, carbon dioxide emissions have been claimed to be the prevalent source of anthropogenic climate change. Studies by the Intergovernmental Panel on Climate Change (IPCC) show that in order to limit the rate of current temperature increase trend, the global CO_2 emission level in 2050 should be reduced by 50-80% of that in 2000 [4]. In addition to emerging ecological concerns, the receding fossil fuel reserves warrant a shift towards low-cost and environmentally friendly energy production alternatives. Options like solar, geothermal, wind, and hydroelectric energy are all potential candidates. However, the intermittent nature of these energy source remains problematic.

The missing links required for a sustainable energy system are an energy storage scheme (a way to store the renewable energy for times when it is not being generated) and an energy carrier (something to replace gasoline and other fossil-derived energy carriers). Energy storage technologies include H_2, batteries, flywheels, supercapacitors, pumped hydro, and compressed gas. However, the most versatile energy storage system and the best energy carrier is H_2. Hydrogen can replace fossil fuels as the energy carrier for transportation and electrical generation when renewable energy is not available. Because H_2 is transportable by gas pipelines or can be generated onsite, any system that requires an energy carrier can use H_2. The conversion of the chemical energy of H_2 to electrical energy by a fuel cell produces only water as waste [5].

Currently, H_2 is manufactured in large quantities from the steam reforming of natural gas (95% of currently-produced hydrogen). However, H_2 can also be generated electrochemically using a commercial electrolyzer coupled with a clean energy source. H_2 is produced at the cathode by splitting water, while O_2 is produced at the anode. In alkaline electrolytes, nickel is used to

make electrolyzer electrodes due to its high electrocatalytic activity and stability, but this metal is highly unstable in the acidic environment due to its rapid corrosion. It should be noted that a much more preferred way of electrolysing water to produce H_2 is in the acidic medium of polymer-electrolyte-membrane (PEM) electrolyzers, due to their significantly higher power efficiencies as compared to currently-used alkaline-based electrolyzers. However, only noble-based metals (Pt, Ir, Ru Pd) work well in PEM electrolyzers.

Platinum-based catalysts are the most active materials for low-temperature water electrolysis. The activities of Pt electrodes in acidic electrolytes considerably exceed those observed in alkaline solutions. Unfortunately, Pt and other noble metals are very expensive (Pt costs over $32 000/kg as of April 3, 2016). Commercial electrode requires a Pt loading from 1 to 4 $mg.cm^{-2}$. Consequently, the catalyst alone can drive up the cost of the electrolyzer above commercially viable prices.

1.2 Rationale and Objective

The high cost of the catalyst materials in acid conditions and possible improvement of performance in alkaline conditions indicate that there is still a need for research in alternative electrodes that can combine high performance with reduced cost. Since in acidic conditions platinum metals remain the most effective and have much higher activity than in the alkaline environment, they have not been ruled out in research despite their elevated cost. A few routes are being actively investigated to improve the electrocatalytic activity of Pt-based catalysts. They consist mainly of alloying Pt with transition metals or tailoring the Pt particle size so a lower loading (amount) of Pt is used, while maintaining the same or achieving a higher electrocatalytic activity.

The work done in this thesis focuses on producing an electrode with reduced platinum loading and tailored particle size. Given that the hydrogen evolution reaction (HER) is a heterogeneous reaction occurring on the surface, the amount of hydrogen produced is proportional to the surface area involved in the reaction. Traditional electrodes use high surface area materials (usually vulcanized carbon powder) as support. The metal's catalyst is then added using wet chemistry or electrochemistry to make nanoparticles. These methods often cause particles to agglomerate and disperse unevenly on the surface. This can reduce the effective area and trap H_2 thus, decreasing H_2 production.

The ***main objective*** of this thesis project is to produce and characterize a low cost, high surface area, and stable electrode with high catalytic activity for the HER. The materials proposed for the elaboration of the electrode have been chosen accordingly. The core structure of the electrode will be composed of multiwall carbon nanotubes (MWCNT) due to their high surface area and electrical conductivity. Additionally, this material has been shown to be stable in electrochemical operations [1]. Platinum nanoparticles will be deposited on the nanotubes. This metal was chosen since it has been extensively studied and is known to be the best catalyst for the HER. The electrode must have a reduced Pt loading in order to maintain cost at an acceptable level.

2 Background and Theory

2.1 Electrocatalysis

The rate of an electrode reaction is characterized by the current density. The effect of various macroscopic parameters on the current is of particular importance in electrocatalysis. Firstly, the composition of the electrolytic solution adjacent to the electrode is one such parameter. The ions in the vicinity of the electrodes under the influence of the electrodes' electric field form what is known as the double layer[6]. Secondly, the rate of reaction is also determined by the nature of the electrode surface. Finally, the rate is strongly dependent on the electrode potential, characterized by the reaction overpotential.

2.1.1 The Double Layer

The double layer is illustrated in Figure 2.1(a). When a metal electrode is brought into contact with an electrolyte, an interfacial region is established, with excess charge carriers of opposite signs on the solution and electrode sides. This region is known as the electrical double layer (DL). On the electrode surface, the charge (in the form of an excess or deficiency of electrons) resides in a thin layer of less than 0.1 Å [2]. It is counterbalanced by cations or anions of the electrolyte that accumulate in front of the electrode, due to Coulombic interactions. Figure 2.1 (b) illustrates the corresponding electrical potential profile across the DL in the absence of chemisorption on the surface. The profile is characterized by a linear drop between the electrode and the Outer Helmholtz Layer (OHL) and a monotonic, nonlinear decay across the diffuse layer, which approaches an exponential decay for small charge densities on the electrode (or voltage drops across the DL not larger than a few tens of millivolts). The presence of chemisorbed species may significantly alter the profile across the DL [2]. Therefore, the nature of the electrode and electrolyte can drastically impact the electrical potential in the DL region. This region is of particular importance as it encompasses the reaction plane. The reaction plane is the location where the reacting species exchange ions or electrons with the electrode. Thus, the electrostatic potential

in the reaction plane varies with the electrode material, and with it, the reaction rate. In this respect, the DL structure is an important aspect of electrocatalysis.

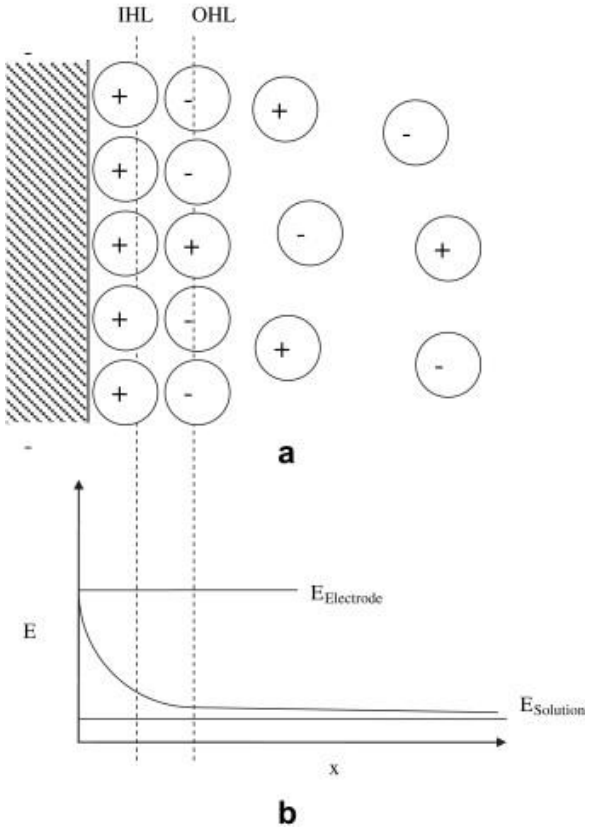

Figure 2.1-A schematic illustration of the electrical double layer and potential distribution near an electrode surface.

2.1.2 Potential in the Electrolytic Cell

The driving force for the current flow in an electrochemical cell is the negative change in Gibbs energy of the overall cell reaction, which in the case of an H_2/O_2 electrolyzer cell is:

Cathode	$2H^+ + 2e^- \leftrightarrow H_2$	(1)
Anode	$H_2O \leftrightarrow 2e^- + 2H^+ + 1/2\ O_2$	(2)
Total	$H_2O \leftrightarrow H_2 + 1/2\ O_2$	(3)

The equilibrium potential of the cell, ΔE_{eq}, then corresponds to the difference in Galvanic (Volta) potentials between the two electrodes, and a Faradaic current flows when the two terminals are connected through a resistor and provided the cell potential is larger than the equilibrium value, defined as:

$$\Delta E_{eq} = -nF\Delta G \quad (4)$$

Thus, when an external voltage greater than ΔE_{eq} is imposed between the two electrodes, electrons will flow and chemical reactions (1) and (2) will occur at the electrodes. For any electrocatalytic reaction to occur an overpotential, η (in volts), must be applied. The overpotential is defined as the extent to which the potential must be driven beyond equilibrium for the reaction to occur [7]. This value is given by the following equation:

$$\eta = E - E_{eq} \quad (5)$$

As a consequence, a higher overpotential causes an increase in power consumption. The overpotential might originate from three sources: activation energies of the electrode reactions (which may originate from the sluggish charge transfer, coupled chemical reactions, etc.), concentration profiles at the electrode owing to mass transport limitations, and ohmic (iR) losses. iR losses (ohmic losses) occur in the cell or in the outer electrical connections. The goal of *electrocatalysis* is to find electrode materials which minimize the activation overpotential.

2.1.3 Current and Reaction Rate

The current is equal to the change of charge with time which is expressed as follows:

$$i = \frac{dQ}{dt} \quad (6)$$

where *i* (in Amperes, A) is the faradaic current, *t* is the time (in seconds, s) and *Q* (in Coulombs, C) is the charge given by Faraday's law seen in the equation below.

$$Q = nFN \quad (7)$$

where *F* is the Faraday constant (*F*=96,485.3 C.mol^{-1}), n is the number of electrons transferred per mole of product/reactant, and N (in moles) is the amount of product formed or reactant reacted. As mentioned previously, electrocatalysis occurs at the electrode-solution interface [7].

Consequently, given that electrochemical reactions are heterogeneous, it is no surprise that the rate of such reactions is dependent on the surface area of the electrode, or more generally on the phase boundary where the reaction occurs. The reaction rate in electrochemical processes is as follows:

$$Rate[mol\,\sec^{-1}\,cm^{-2}] = \frac{i}{nFA} = \frac{j}{nF} \tag{8}$$

where j (in A.cm^{-2}) is the current density.

There are four major factors that govern the reaction rate and current in electrodes: mass transfer to the electrode surface, kinetics of electron transfer, preceding and ensuing reactions, and surface reactions (adsorption) [7]. These processes are illustrated in Figure 2.2. Consider the sample reaction:

$$O + ne^{-} \leftrightarrow R \tag{9}$$

For this reaction to proceed, the oxidized species O must move from the bulk solution to the interface of the solution with the electrode. This aspect of the reaction is governed by mass transfer equations such as Fick's law of diffusion and the Nernst-Planck equation, which will be discussed in later sections. This process can be rate-limiting for the reaction. However, when evaluating an electrocatalyst it is important to ensure that mass transfer is not limiting so as to study the electrode phenomena occurring. When all of the processes leading to the reaction are fast, this leaves the electron transfer reaction as the limiting factor.

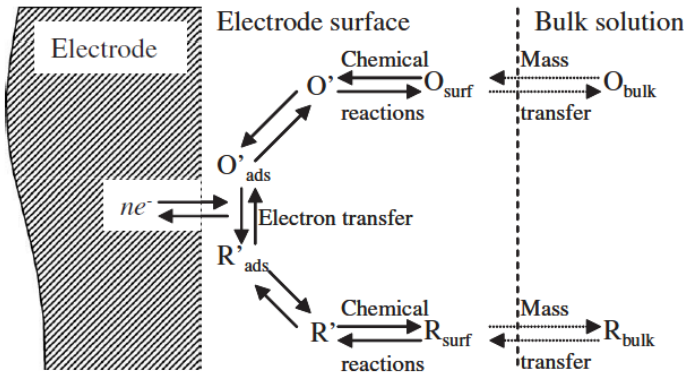

Figure 2.2- Processes involved in electrode reactions

2.1.4 Kinetics

In this section it will be assumed that mass transport phenomena are not limiting so as to focus on the electron transfer processes. When investigating the properties of a catalyst experimentally, it is preferable that this assumption be valid. In such a case, the concentration of the electroactive species at the outer Helmholtz layer is the same as in the bulk of the solution. We will consider the electron transfer process mentioned in the previous section:

$$O + e^{-} \leftrightarrow R \tag{10}$$

This reaction may seem like an oversimplification of electrode processes; however, this is not necessarily the case. In general, we expect that any electrode process involving two or more electrons necessarily involves two or more elementary steps. This is due to the fact that the addition of two or more electrons in a single step is highly unlikely [8]. Now consider that the rate of the forward reaction (cathodic or reduction reaction) is first order with respect to O and that the reverse (anodic or oxidation reaction) is first order with respect to R. Consequently, when the rates are combined with equation (8) the anodic and cathodic currents are as follow:

$$i_c = FAk_cC_O(0,t) \tag{11}$$

$$i_a = FAk_aC_R(0,t) \tag{12}$$

where F is Faraday's constant, A (in cm^2) is the area of the electrode, and $C(x, t)$ (in $mol.cm^{-3}$) is the concentration of species (R or O) at distance x (in cm) from the electrode at time t (in seconds). Here we are considering reactions at the electrode surface, therefore $x = 0$. The temperature dependence of the rate constants k_a and k_b follows the Arrhenius kinetics and is thus given by:

$$k_c = k_0 exp\left(-\frac{\alpha F(E_e - E^{\circ})}{RT}\right) \tag{13}$$

$$k_a = k_0 exp\left(\frac{(1-\alpha)F(E_e - E^{\circ})}{RT}\right) \tag{14}$$

where R is the gas constant, T is the temperature and the transfer coefficient, α, is a dimensionless parameter, and k_0 is a constant. When a net current flows through the electrochemical cell, the cell is not at equilibrium. The half-cell potential deviates from the equilibrium value by the overpotential η. Substituting this value in the rate constants we obtain the following expressions:

$$k_c = k_{c,0} exp\left(-\frac{\alpha F\eta}{RT}\right) \tag{15}$$

$$k_a = k_{a,0} exp\left(\frac{(1-\alpha)F\eta}{RT}\right) \tag{16}$$

Thus the net current in the cell is the sum of the anodic and cathodic current, and is as follows:

$$i = FA\left[k_{c,0} C_O(0,t) exp\left(-\frac{\alpha F\eta}{RT}\right) - k_{a,0} C_R(0,t) exp\left(\frac{(1-\alpha)F\eta}{RT}\right)\right] \tag{17}$$

Or

$$i = i_0\left[\frac{C_O(0,t)}{C_O^*}\, exp\left(-\frac{\alpha F\eta}{RT}\right) - \frac{C_R(0,t)}{C_R^*} exp\left(\frac{(1-\alpha)F\eta}{RT}\right)\right] \tag{18}$$

where i_0, the exchange current, is equal to the cathodic current (and to the negative of the anodic current) at equilibrium and C_O^* and C_R^* are the bulk concentrations. If the transport is sufficiently fast that $C_O(0,t) = C_O^*$ and $C_R(0,t) = C_R^*$, then the equation reduces to

$$i = i_0\left[exp\left(-\frac{\alpha F\eta}{RT}\right) - exp\left(\frac{(1-\alpha)F\eta}{RT}\right)\right] \tag{19}$$

This equation is known as the Butler-Volmer equation after the two electrochemists who, in 1924 and 1930, respectively, contributed to its formulation and experimental validation.

The Butler-Volmer equation is used to analyze the electrode kinetic data by summarizing this information in two parameters, the exchange current i_0 (or exchange current density j_0) and the transfer coefficient α (it should be noted that the equation applies only if the electron-transfer is a slow step, i.e. the reaction is under activation control; this generally applies to the hydrogen evolution reaction from aqueous solutions).

The transfer coefficient α, which was introduced earlier, is used to separate the potential contribution to the free energy of the cathodic reaction from the contribution to the free energy of the anodic reaction. The significant role of this parameter is illustrated in equations 17 and 18. It reflects the dependence of k_c and k_a on the overpotential. To exemplify this point, if we take α=0, 1-α=1, the cathodic free energy of activation (and thus the cathodic current) would be independent of overpotential, and all the variation of the net current from the potential would be through the anodic component. Similarly, if α =0.5 and 1-α=0.5, the anodic and cathodic currents would respond symmetrically to changes in the overpotential.

The exchange current is a relevant parameter in comparing the catalytic activity of electrodes. However, in the case where multiple parallel electrochemical reactions occur at an electrode, it cannot reveal which portions of the current contribute to any given reaction. Nevertheless, the exchange current remains the most adequate method to compare the overall catalytic activity of electrodes from a fundamental research point of view. From the engineering perspective, however, it is not quite the same. Since energy is consumed in the form of power, overpotential plays a more prevalent role in the comparison of electrocatalysts. In this case, a comparison of the overpotential developed at a useful (working) current density is used to determine which catalysts are more efficient. The transfer coefficient plays an important role here, as it determines the efficiency at which overpotential is used for a given electrode process. In the case of H_2 reduction, a transfer coefficient closer to 1 would be desirable since it is a cathodic process [9].

The most common method to obtain these parameters from experimental data in a well-mixed solution is through the analysis of current-potential curves. When the overpotential is sufficiently large (i.e. abs($F\eta/RT$)>>1) one of the exponential terms of equation (19) becomes negligible compared to the other [7, 8]. At this point taking the logarithm of the current yields the following expression for a cathodic reaction:

$$\ln i = \ln i_0 - \frac{\alpha F}{RT}\eta \quad (20)$$

This equation is known as the Tafel equation. This equation provides the means to determine the exchange current and transfer coefficient. It suggests that current increases exponentially with increasing overpotential [7], and that there must be a point at which the current becomes limited by the rate of transport and the current versus potential plot begins to flatten out. The point at which this happens depends partly on the efficiency of stirring and on the diffusion coefficients of the electroactive species, but more critically on the electron-transfer rate. For slow electron-transfer processes the exchange current is so small that the rate of transport is rarely a problem. For faster processes, however, the Tafel plot approach may be impractical because, with increasing overpotential, transport limitation sets in before the linear Tafel region has been established [8].

2.2 Hydrogen Evolution Reaction (HER) in Electrocatalysis

2.2.1 Mechanism of HER

The hydrogen evolution reaction was the first electrochemical reaction to be investigated in the 1800s. It has been extensively studied since then for a wide variety of systems. The overall reaction in acid electrolytes (equation 21) and in alkaline electrolytes (equation 22) are :

$$2\mathrm{H}^+ + 2e^- \rightarrow H_2 \quad (21)$$

$$2\mathrm{H}_2O + 2e^- \rightarrow H_2 + 2OH^- \quad (22)$$

HER is a complex multielectron–multistep electrochemical reaction, involving charge transfer steps, chemical reaction steps, and also the mass transport of H_2 and H^+ from and to the electrode surface. It is generally accepted that there are three possible steps in the HER, which are presented in equations (23) -(25). Here the symbol M represents free adsorption sites on the catalytic surface. Equation (23) is known as the Volmer step, equation (24) is the Tafel step, and (25) is the Heyrovsky step. These steps are combined to propose reaction routes for the HER. There are two generally accepted reaction sequences through which the HER can occur: the Volmer-Tafel or the Volmer-Heyrovsky reactions [10].

Volmer	$M + H^+ + e^- \leftrightarrow M - H_{ads}$	(23)
Tafel	$2M - H_{ads} \leftrightarrow H_2 + 2M$	(24)
Heyrovsky	$M - H_{ads} + H^+ + e^- \leftrightarrow H_2 + M$	(25)

The kinetic equation for the HER, and hence the dependence of the overall current on the electrode potential, vary markedly depending on which reaction is the rate-determining step (RDS). In order to determine the reaction mechanism of the HER, some key electrochemical parameters must be determined experimentally. These parameters include the exchange current density j_0 in A.cm^{-2} at a given temperature and pressure, the corresponding activation energy, the anodic and cathodic transfer coefficients α, and the Tafel slopes in mV.dec^{-1}. These parameters would reveal which among the Tafel, Volmer and Heyrovsky reactions constitutes the rate-determining step [11].

The most intensively studied experimental parameters have been the Tafel slope and exchange current density. For Pt in acidic electrolytes, it has been reported that j_0 values fall into the range of ≈1 mA.cm^{-2} with anodic and cathodic Tafel slopes ranging from 30 mV.dec^{-1} to 120 mV.dec^{-1}. In alkaline electrolytes, Tafel slopes ranging from 50 to 140 mV.dec^{-1} have been reported [12]. The formation of the adsorbed hydrogen atom (Volmer step) as the first step is common to both mechanisms. Hence when this is the rate-determining step we cannot be certain of the overall mechanism. The Tafel slope in this case is 120 mV.dec^{-1}. In the cases where a Tafel slope of 30 mV.dec^{1} is obtained, the RDS is the Tafel step where two adsorbed hydrogen atoms react to form hydrogen gas. The overall mechanism in that case is the Volmer-Tafel. The Volmer-Heyrovsky can be identified when a slope of 40 mV.dec^{-1} is obtained. In that case, the RDS is the Heyrovsky step in which one adsorbed hydrogen atom reacts with an H^+ in a solution of hydrogen gas [13, 14].

2.2.2 Metal Catalysts for the HER

The HER has been studied on a multitude of metals and alloys. The exchange current density, which is an indicator of the activity of a catalyst toward the HER, has been shown to vary by up to 10 orders of magnitude. Bockris [15] was the first to discuss dependence of the HER on the metal work function Φ. However, it was Trasatti who demonstrated that the logarithm of the exchange current density, $\log j_0$, varies linearly with the metal work function Φ, irrespective of the detailed nature of the mechanism involved in the rate-determining step [16, 17]. In addition, Trasatti showed that transition metals and *sp* metals with positively charged surfaces and *sp* metals with negatively charged surfaces fall on two different straight lines that are shifted in parallel along the Φ axis. The shift has been interpreted in terms of differing orientations of water dipoles at the interface of the two groups of metals [2].

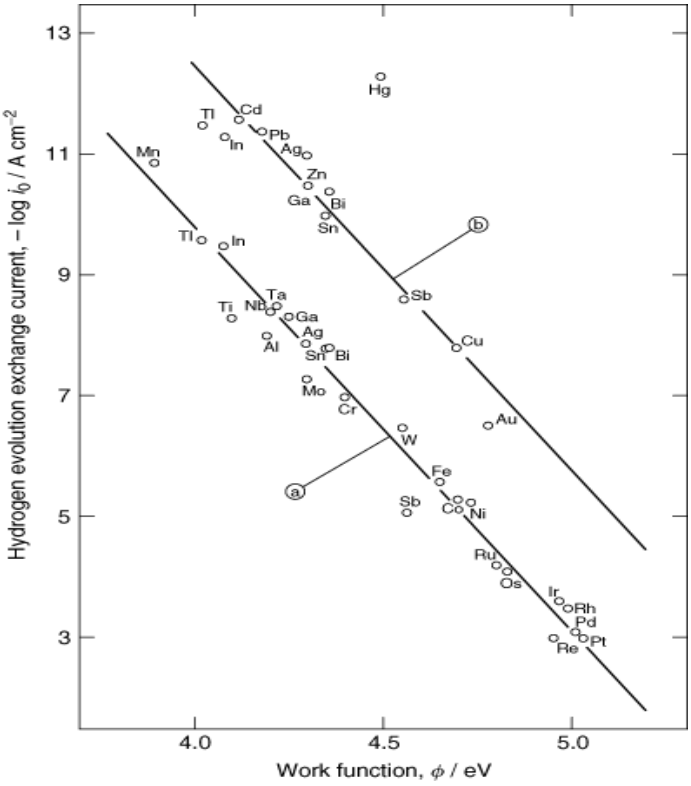

Figure 2.3- Exchange current densities for the HER versus work functions of metals: (a) refers to transition metals and sp metals with positively charged surfaces and (b) refers to sp metals with negatively charged surfaces

Conway and Bockris later demonstrated that the linear relationship observed between log j_0 and Φ was due to the correlation between the work function and the adsorption energy between hydrogen atoms and the surface of the metals. This observation gave rise to volcano curves, Figure 2.4. The most widely used volcano curve correlates log j_0 and the heat of adsorption of hydrogen on metals [2]. Pt possesses the highest catalytic activity for HER and exhibits high current densities in the vicinity of the equilibrium potential.

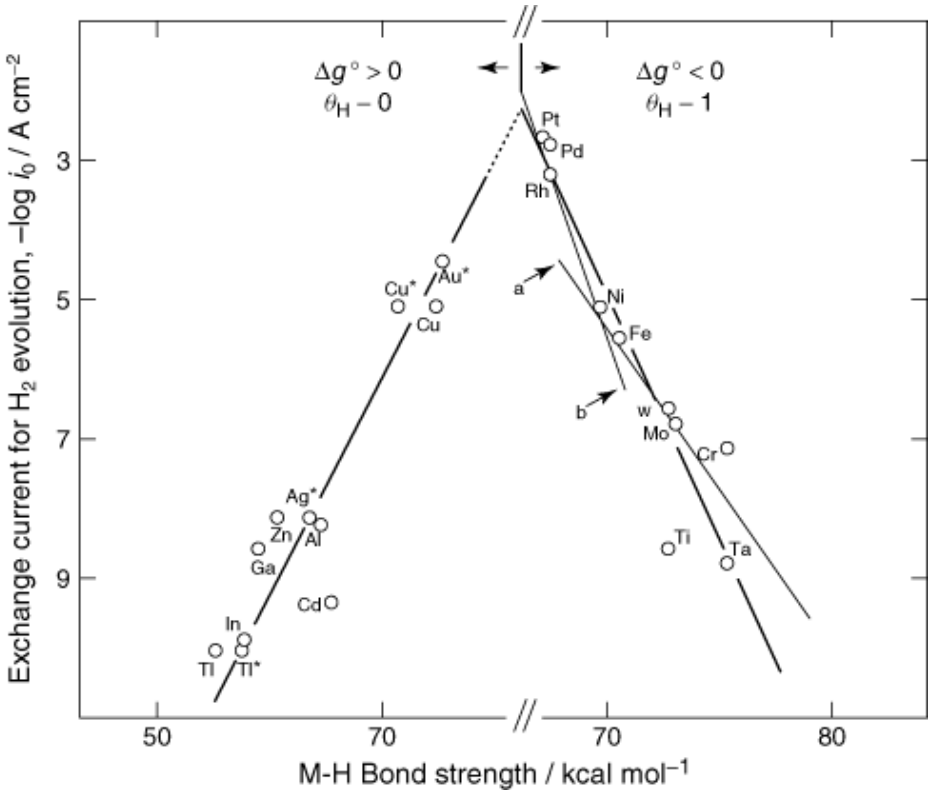

Figure 2.4-Exchange current densities for the HER vs. strength of M-H bond

2.3 Carbon Nanotubes

The discovery of carbon nanotubes (CNTs) is attributed to Iijima [18]. He reported in a 1991 publication in *Nature* his work on hollow nanosized tubes of graphitic carbon. Discussions and studies of CNTs have gained momentum since their discovery, owning to their unique and highly sought-after properties. CNTs are the essential building block of the electrocatalyst synthesized and studied in this work. Consequently, comprehensive knowledge of CNTs is an integral part of this thesis.

2.3.1 Electronic Structure

Graphite is a well-known hexagonally structured form of carbon composed of layers of sp^2 bonded carbon atoms. This honeycomb-like structure can be seen in Figure 2.5 (a). The different carbon layers in graphite interact weakly, primarily through van der Waals forces. This interaction produces a small valence and conduction band overlap of about 40 meV, which makes graphite overall a semi-metal. Each hexagonal lattice plane of graphite is composed of a single sheet of graphene. There are about 3 million layers in a millimeter thickness of graphite.

Graphene, which is essentially a single sheet of graphite, retains similar structural properties as graphite, including sp^2 bonded carbon. However, the electronic structure of graphene is quite different. Graphene exhibits a peculiar single-particle energy band structure which causes charge carriers (i.e. electrons and holes) to have zero effective mass and a velocity that is about 300 times slower than that of light [19].

The electronic structure of CNTs is usually discussed on the basis of the band structure of graphene. Single wall carbon nanotubes (SWCNTs) are considered to be formed by rolling a sheet of graphene into a cylinder. Therefore, the remarkable electrical properties of CNTs have their origin in the unusual electronic band structure of graphene. The diameter and helicity of a SWCNT are uniquely characterized by the roll-up vector $\mathbf{C}_h = n\mathbf{a_1} + m\mathbf{a_2}$ that connects crystallographically equivalent sites on a two-dimensional (2D) graphene sheet, where $\mathbf{a}_1$ and $\mathbf{a}_2$ are the graphene lattice vectors and n and m are integers ((b)). The limiting, achiral cases, (n, 0) zigzag, and (n, n) armchair are indicated with dashed lines in (b). The translation vector **T** lies along the tube axis and is orthogonal to $\mathbf{C}_h$, and its magnitude represents the length of the unit cell of an (n, m) tube. The rolled-up area swept out by **T** and $\mathbf{C}_h$ corresponds to the repeat unit of an (n, m) tube; hence, a nanotube's (n, m) symmetry determines the size of its unit cell, which can vary greatly among tubes. Electronic band structure calculations predict that the (n, m) indices determine whether a SWCNT will be a metal without a bandgap or a semiconductor with a bandgap. Zigzag SWCNTs, represented by the wrapping index (n, 0), can be either metallic or semiconducting, while armchair configuration SWCNTs with wrapping index (n, n) are always metallic [20].

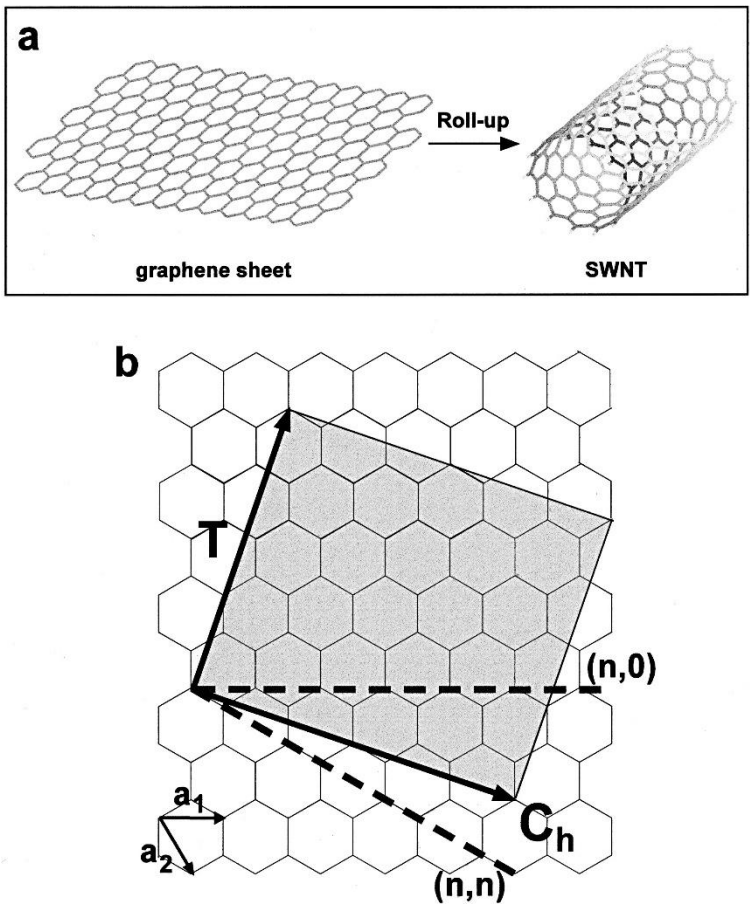

Figure 2.5-Schematic of a 2D graphene sheet illustrating lattice vectors $\mathbf{a}_1$ and $\mathbf{a}_2$ and the roll up vector $\mathbf{C}_h = n\mathbf{a}_1 + m\mathbf{a}_2$. The limiting, achiral cases of (n,0) zigzag and (n, n) armchair are indicated with dashed lines. The translation vector **T** lies along the nanotube axis and defines the 1D unit cell. The shaded, boxed area represents the unrolled unit cell formed by **T** and $\mathbf{C}_h$. The diagram is constructed for (n, m) = (4,2) [21].

2.3.2 CNT Properties

There are two main types of CNTs: single-wall and multi-wall, as seen in Figure 2.6. As stated in the previous section, SWCNTs are a single sheet of graphene rolled up in a cylinder with its ends either open or caped with a semicircle. Typically, SWCNTs are 0.2 to 5 μm in length while their diameter varies between 1 to 2 nm. MWCNTs possess outstanding strength and thermal conductivity at room temperature. They have a very large surface area per unit mass and unique optical properties. The structure of individual graphene tubes is defined by the unit cell where the

open ends may have zigzag, armchair, and chiral geometries as mentioned before. Their electrical properties will vary with chirality.

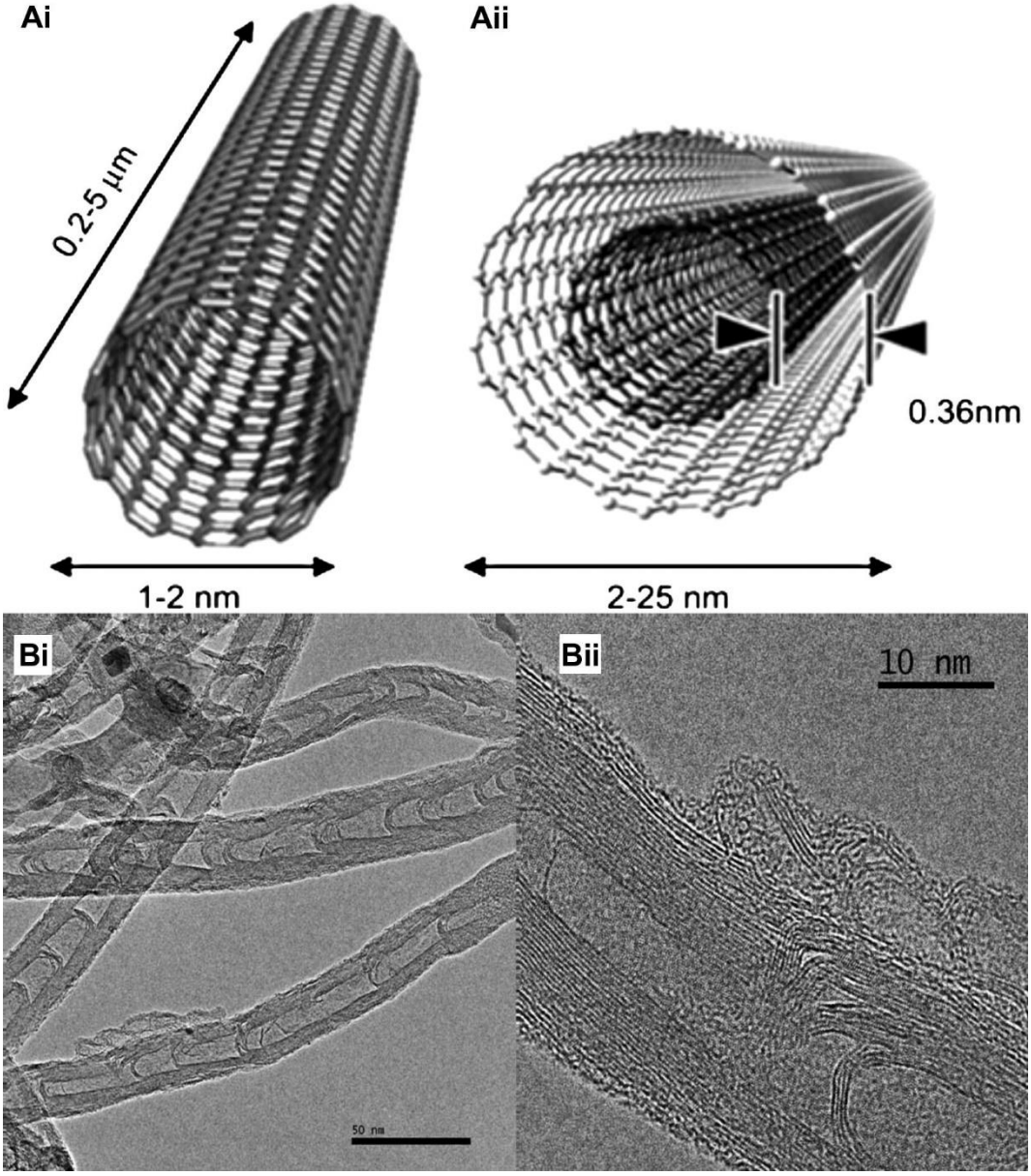

Figure 2.6-A) A conceptual diagram of i) SWCNT and ii) MWCNT showing typical dimensions of length, width, and separation distance between graphene layers in MWCNTs. B) TEM micrographs: i) MWCNT, and with magnification in ii) structure [22]

A MWCNT is considered to be a coaxial assembly of cylinders of SWCNTs, like a Russian doll, one within another. The separation between tubes is about equal to that between the layers in natural graphite. MWCNTs can attain a length greater than a millimeter with a diameter ranging

from 2 to 100nm. The concentric graphene shells in MWCNTs are spaced by 0.36 nm (this distance is similar to the spacing of graphite sheets 0.335 nm). The reported tensile strength of MWCNTs is an outstanding 63 GPa, which equates to a cable of 1 mm^2 in diameter capable of enduring tension caused by a load of 6422 kg. Although MWCNTs demonstrate tremendous tensile strength, they possess less strength under compression due to their hollow nature, which can result in buckling of the CNT structure. The hardness of CNTs determined experimentally is also somewhat outstanding, with a standard SWCNT being capable of withstanding pressures of up to 24 GPa without any deformation. At greater pressures the CNT is found to undergo transformation to a super hard-phase nanotube, which further withstands pressures, currently limited by experimental techniques, of around 55 GPa [22]. Furthermore, MWCNTs are always metallic. MWCNTs have similar current carrying capacity as metallic SWCNTs, but are easier to fabricate than SWCNTs due to easier control of the growth process [23].

2.3.3 Fundamentals of CNT Synthesis

Although a vast array of techniques exists for the synthesis of CNTs, four techniques are most commonly utilized: arc discharge, laser ablation, plasma torch deposition and chemical vapor deposition (CVD). These techniques will be briefly discussed in this subsection, with a strong emphasis on chemical vapor deposition, given that this method was chosen to produce the CNTs used in this project.

Synthesis of carbon nanotubes by arc discharge and laser ablation occurs through the condensation of hot gaseous carbon. The energy from the arc or the laser is used to vaporize a graphite electrode or target. These techniques can produce high-quality SWCNTs and/or MWCNTs at the gram level. In arc discharge, MWCNTs are found within the carbon soot of the graphitic electrode [24]. The anode is usually filled with transition metal catalysts such as Fe, Co, and Ni, which are favorable for the formation of SWCNTs. In laser ablation, an intense laser pulse hits a graphite target and material is removed. During this process an inert gas is bled into the reaction chamber, resulting in nanotubes forming on the cooler surfaces of the reaction chamber as the carbon vapor condenses. The method of laser ablation has been developed from existing methodologies for the production of metal molecules through exposure of bulk metal to a laser, with the bulk metal being replaced by graphite for the synthesis of MWCNTs. The production of SWCNTs is achieved through this same method with a composite target of graphite

and metal catalyst particles. These techniques suffer from drawbacks linked to the equipment requirement and the large amount of energy consumed. Furthermore, only powdered samples with nanotubes tangled into bundles can be produced. Controlled synthesis on substrates with ordered nanotube structures has not yet been achieved with these methods.

The plasma torch based methods for the production of CNTs are highly scalable to industrial applications and offer a high degree of control on the quality of the CNTs produced. In this technique a carbon contain gas is injected into a DC plasma flame. This gas is dissociated in the plasma environment to provide the atomic carbon for CNT growth. In order for CNT growth to nanometer sized catalyst must be present in the jet. In plasma torch process the catalyst particles are produced in-situ through the vaporization of metal electrodes followed by the nucleation of the vapor into nanoparticles in a zone of nanotube formation. The amount of catalyst nanoparticles and of carbon precursor for CNT growth are controlled independently making it a very easily controlled process.[25]

CVD is the technique most readily used in commercial environments due to its ease of implementation and relatively low equipment requirement, especially for systems operated at atmospheric conditions like the one used in this project. In CVD, a substrate is prepared with a layer of catalyst particles, usually nickel, cobalt, iron or, in some instances, a combination of these metals. With the application of heat in the presence of a gaseous or volatile carbon compound, heterogeneous reactions take place on the substrate which produce solid and volatile products, among which are CNTs. The size of nanotubes to be grown correlates with the size of the metal particles used in the synthesis, enabling accurate control of CNT size in terms of both length and tube diameter.

The growth mechanism of MCNTS through CVD was summaries by Kumar et al. [26]. In CVD a hydrocarbon gas decomposes at temperatures between 600 ºC and 1000 ºC, over a metal catalyst. The catalyst is typically composed of nanoparticles of transition metals such as iron, nickel and cobalt due to the limited solubility of carbon in these materials. The nucleation of the CNTs occurs at the eutectic point of these transition metals as absorption and diffusion into the metal particle, results in a carbon-induced liquefaction of the catalyst. The size of the particles plays a crucial role in the process as is has been shown that eutectic temperature of transition metal

are lower for particles below 10 nm [27]. As the hydrocarbons decomposes at the surface of the metal, adsorbed carbon begins to dissolve inside the catalyst. As the carbon dissolves in the catalyst particles carbon diffuses in the nanoparticles due a concentration gradient and precipitated at another location on the particles. Sinnott et al. [28] proposed a model in which the deposition of carbon takes place on only one half of the particle surface (the lower curvature side for the particles). The carbon diffuses along the concentration gradient and precipitates on the opposite half, around and below the bisecting diameter. However, it does not precipitate from the apex of the hemisphere, which accounts for the hollow core that is characteristic of CNTs. For spherical metal catalyst particles, carbon filament forms through two methods, root growth or tip growth [22]. In extrusion growth (also known as root growth), the nanotube grows upward from the metal particle that remains attached to the substrate. In tip growth, the particle detaches from the support and moves to the head of the growing nanotube. A schematic representation of both mechanisms is shown in Figure 2.7. CVD, when optimized to fabricate CNTs, generally results in MWCNTs or poor quality SWCNTs. The SWCNTs produced with CVD have a large diameter range, which is not easily controlled. However, this method is easy to scale up, which is advantageous for commercial production.

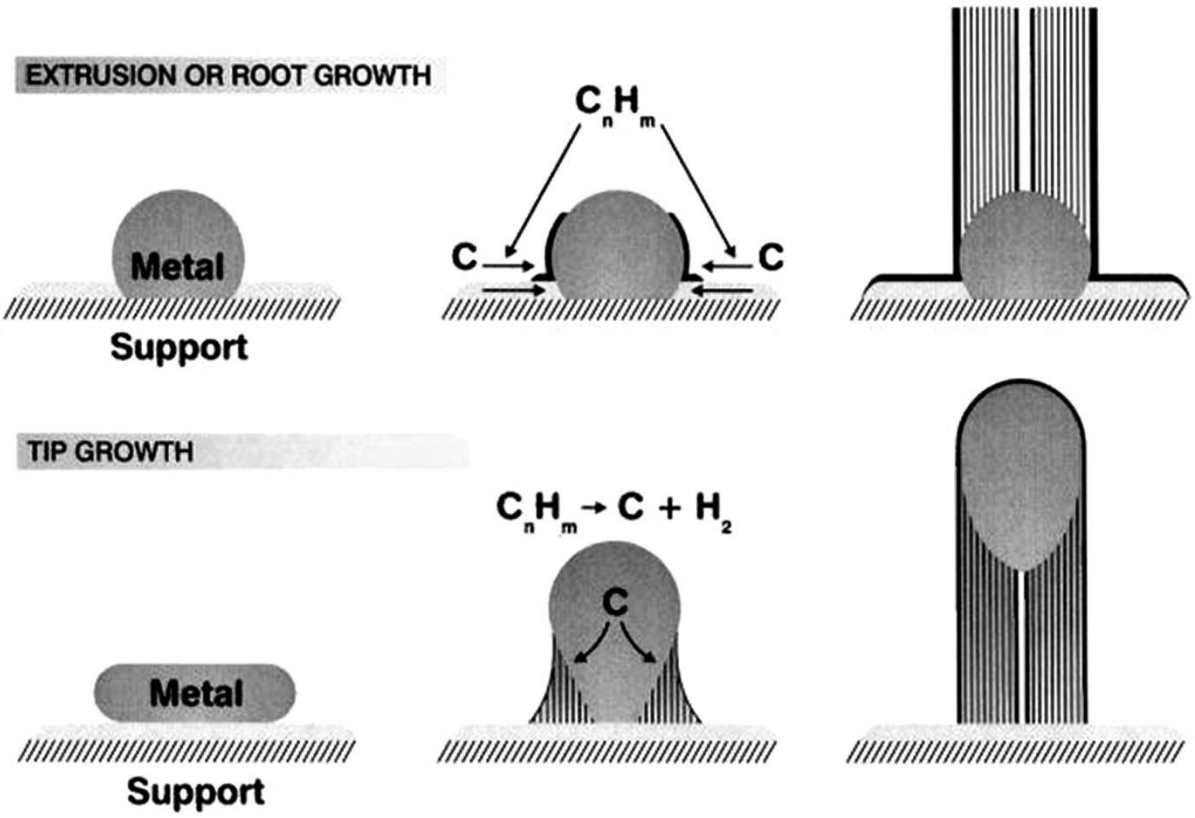

Figure 2.7-Schematic of tip-growth and extrusion mechanisms for carbon filament growth via CVD

The direct growth method used in this project varies from the usual CVD growth methods were nanoparticles of catalyst material are deposited on a substrate. In the method used here a simple SS 316 mesh is used directly for growth. However, the mesh undergoes a heating pretreatment which cause the formation and migration to the surface of nanoscale iron particle in the SS 316 matrix. For the purpose of this project, the ability of CVD to grow the desired MWCNTs directly on a chosen substrate is of great benefit over other methods in which nanotubes must be collected. In addition, the fact the growth substrate is a highly conductive metal (SS 316) is very advantageous. The growth substrate can act directly as a current collector in electrochemical devices, thus removing the need for binder, which can negatively affect the conductivity of electrodes.

2.4 Laser Ablation

The platinum nanoparticles synthesized in this project were produced via a popular bench scale technique known as pulsed laser ablation (PLA). A laser is a device that amplifies light and produces a highly directional, high-intensity beam with a narrow wavelength range. Laser is an acronym for Light Amplification by Stimulated Emission of Radiation. The product of laser ablation will vary according to the operating and environmental conditions and the material being ablated. Therefore, a good understanding of the processes involved in the production of nanoparticles by PLA is essential to this work. This section will first briefly describe the physics and operation of a Nd-YAG laser. Then the processes involved in the ablation of material with a laser will be presented. Finally, the processes controlling the formation of nanoparticles will be explained.

2.4.1 Laser Fundamentals

When discussing the interaction of lasers with material, it is important to understand both the wave nature of light and its quantum nature. The quantum theory of light states that light is quantized in discrete bundles of energy called photons. When electrons in atoms or molecules transition from an excited energy state to a lower energy state they radiate an exact amount of energy. That exact amount of energy is thought of as a single bundle of energy because of its discrete nature. Although light is packaged in discrete photons, light has a wave nature characterized by frequency and wavelength. Therefore, each photon has an associated energy level that depends on its frequency, as can be seen from the Planck relationship [29]:

$$E = E_2 - E_1 = h\omega$$

where E_2 and E_1 are upper and lower energy levels respectively, h is the Planck constant (h=6.626×10^{-34} J.s) and ω is the frequency of oscillation.

As mentioned previously, electrons or molecules can reach lower energy levels by emitting a photon. Conversely, the jump to a higher energy state can be stimulated by a photon. There are three energy transition processes that are of interest in laser physics: stimulated absorption, stimulated emission, and spontaneous emission.

Stimulated absorption, also refereed to resonate absorption, denotes the process by which an atom or molecule absorbs an energy of $h\omega$ from a proton when subject to an electromagnetic

field of frequency ω [30]. As a result, the atom or molecule is raised from the energy state *n* to a higher state *m*. This process can only occur if the energy gap separating the two states exactly matches the energy of the photon. This process is schematically illustrated in Figure 2.8 (a). This excited state is usually unstable. Therefore, nano- or picoseconds later, the excited species returns to its lower emission state by emitting a photon. This process, known as spontaneous emission, is illustrated in Figure 2.8 (b). In spontaneous emission, the photon emitted is not connected to the incident radiation in any way. The incident radiation does not affect the lifetime of the excited state of the molecule that emits the spontaneous emission. In addition, the emitted photons have no definite phase relation to each other. The last radiative process seen in Figure 2.8 (c) is the most important for the operation of a laser. In the case of stimulated emission, an incident photon interacts with a molecule or atom already at a high energy level *m*. The exited molecule or atom then returns to a lower energy level, emitting a photon with identical characteristics to that of the incident radiation [29].

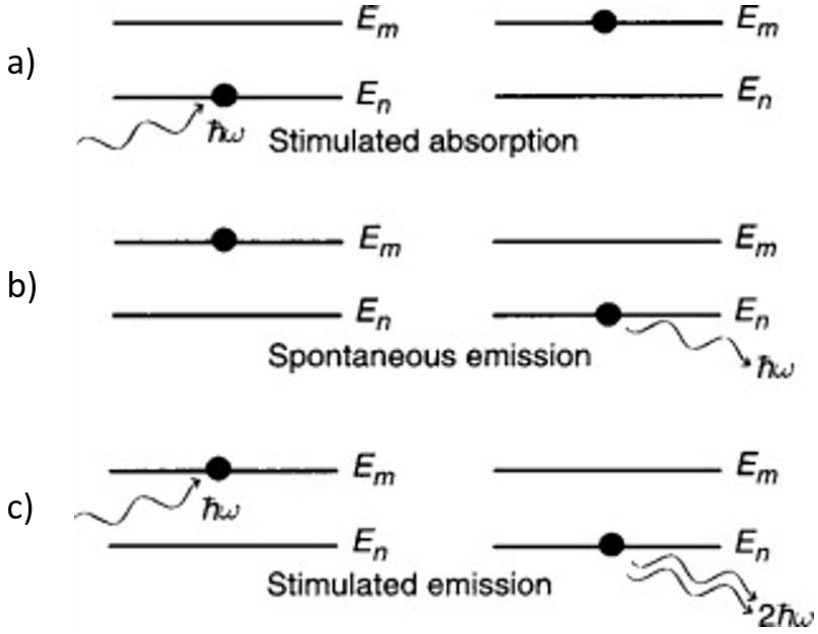

Figure 2.8-Scheme of a two-level system illustrating: a) stimulated absorption, b) spontaneous emission, and c) stimulated emission phenomena.

However, stimulated transition can only occur when the external radiation field is in resonance with the transition level, which is equivalent to satisfying the Planck relation. The properties of

stimulated emission are key to the functioning of lasers. To begin with, the incident radiation and the radiation generated by the stimulated emission have the same frequency, phases, plan, and direction of propagation. In addition, the probability of a stimulated transition per time unit is proportional to the energy density of the external field.

In order to sustain an output, that lasing material must have more species occupying upper energy levels than the ground state. This phenomenon is known as population inversion. The process used to raise molecules to the excited state is called pumping [31].

2.4.2 Laser Operation

The basic laser structure consists of an active optical gain medium that amplifies electromagnetic radiation, a pumping source that pumps energy into the active medium, and an optical resonator that is composed of two highly reflective mirrors. As the pump process raises molecules in the gain medium to excited states until population inversion is achieved, lasing is initiated by spontaneous emission and amplified by stimulated emissions along the axis of the resonator cavity. The cavity mirrors reflect the photons back and forth through the laser to increase amplification.

The gain medium in a Nd-YAG laser is an assemblage of crystal rods of neodymium (Nd^{3+})-doped YAG (yttrium aluminum garnet, $(Y_3Al_5O_{12})_{13}$. The pumping in this case is done by a flashlamp. The schematic of this laser can be seen in Figure 2.9 [31]. The flashtube (F) is placed in one focus of an elliptical cylinder (cavity), the rod (R) being placed in the second focus. The flashtube is supplied by power supplies for high voltages, E (~1,000 V), using capacitors, C, and resistors, R. A particularity of this solid state laser is that its frequency can easily be doubled or tripled through harmonic generation to create shorter wavelength protons, usually at the expense of some output energy. However, q-switching can mitigate losses by emitting a pulse train of higher peak power pulses than continuous wave output. During the pumping process, photons emitted by spontaneous emissions in directions other than the axis of the resonator cavity are amplified. These photons are not reflected back in the cavity, and are therefore lost in the environment. The loss of photons travelling off axis is termed amplified spontaneous emission (ASE). Q-switching is a pulse enhancement technique used to minimize these losses. This technique employs an electronic shutter called a Pockels cell which is triggered open and shut using an electrical switch.

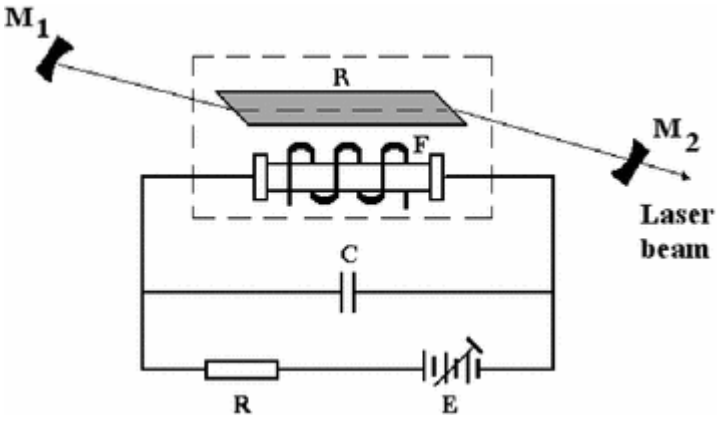

Figure 2.9-Schematic of Nd-YAG laser

In order to produce beams of different wavelengths, harmonic generation is used with Nd-YAG lasers. This process requires the use of materials that exhibit nonlinear effects when irradiated with high-intensity emissions. The electric dipole established by the electrons and the nuclei of these materials oscillate in response to incident radiation so that two separate wavelengths of light exit the materials. The output of these materials includes the original wavelength(1054 nm for Nd-YAG) and a component half the wavelength of the incident beam [29]. The second harmonic generation of Nd-YAG lasers results in light output at 532 nm wavelengths in the green portion of the visible spectrum, while the third harmonic generation causes an output of 355nm.

2.4.3 Nanoparticle Production

PLA is the process by which material is removed under the action of short and focused laser pulses. During this process, heating, melting, vaporization, and ionization of the target material takes place [31]. Metals, semiconductors, and insulators can all be deposited on a substrate using this technique. PLA becomes effective when the laser fluence is larger than the threshold value F_{th}, which results in removal of at least one mono-atomic layer. The fluence of a laser pulse is the optical energy delivered per unit area. Its most common units are $J.cm^{-2}$. The ablation process produces a very hard-to-control and unpredictable mixture of atoms, ions, clusters, and droplets. Thus, the only possible approach for particles fabrication by pulsed laser ablation is a mild laser-target interaction producing only atoms or very small clusters. The nanoparticles grow into the ablation plasma during plume propagation. The growing process will be controlled by the ablation process' ambient conditions [31].

The nanoparticle formation mechanism has two distinct elementary steps: the nuclei formation and the nanoparticles' growth process over the formed nuclei. The number of nuclei per unit volume mostly depends on the pressure, temperature, and amount of material available. The nuclei formation and particle growth processes are concurrent and competing processes, as they both consume the vaporized material [32]. Therefore, for nanoparticle production, the process parameters that lead to nanoparticle formation must maximize the nuclei formation rate relative to the particle growth rate.

The main control parameter in the nanoparticle fabrication process is the cooling speed. The nanoparticle size distribution is rather close to a lognormal function; therefore, the cooling rate influence on the particle size distribution will control the particle size dispersion. The cooling speed can be influenced in several ways. It can be influenced by changing the amount of ablated material present by controlling the laser power or changing the ambient gas type. However, the most convenient control parameters for nanoparticle fabrication by PLA are temperature and pressure. Studies [31] done on the nanoparticle formation process indicate that as the temperature decreases, the nuclei generation process is increased with a higher rate than the particle growth rate. Therefore, a faster cooling speed will result in a higher number of smaller-size particles. In addition, the growth rate decreases with the decrease of ambient pressure, thus causing the nanoparticle size distribution shift toward smaller dimensions.

PLA is very good technique for nanoparticle production due to the narrow size distribution that can be obtained. However, since the distribution of size is always lognormal, it is impossible to completely remove the large-size particles that are also produced. Another advantage of PLA is the high purity of the particle produced. The nanoparticles produced by PLA do not present any contamination since laser ablation preserves the purity of the target material.

3 Experimental Methods

3.1 Electrode Fabrication

3.1.1 Carbon Nanotubes

In this project, MWCNTs are the backbone of the composite electrode used in the reduction of hydronium ions to hydrogen gas. The procedure used for their synthesis is based on the initial

work of Baddour et al. [3]. MWCNTs are growth directly on a 316L stainless steel (SS) substrate without the addition of nanoparticle catalysts. The direct growth process results in the formation of MWCNTs covalently bonded to the SS substrate. This enhanced electrical contact and provided optimal electron transport from the MWCNTs to the growth substrate, thus making the SS substrate an ideal current collector for the composite electrode. Having the MWCNT directly bounded on the current collect improved the electrical conductivity over electrode that require binding substances. The procedure was later improved by Hordy et al. [33, 34]. The MWCNTs form a dense forest on the SS substrate, with an average diameter and length of approximately 30 nm and 4 μm, respectively [35]. Austenitic iron (with a eutectic point) in the substrate acts as a catalytic site for the MWCNTs. The presence of relativity large iron particles (around 30 nm) in the middle section of the MWCNTs indicate that there may be a combination of root and tip growth involved in their formation.

In this subsection, a brief description of the thermal chemical vapor deposition (t-CVD) setup will be followed by an outline of the experimental procedure. More details can be found in the work of Hordy et al. [33]. The setup consists of an electrical tube furnace (Linderg-Blue HTF 5500; 120V/30A) through which passes a quartz tube with an internal diameter of 5.5 cm and a length of 1.22 m. About 53 cm of the central section of the tube is heated in the furnace while the tube ends are exposed to ambient air. The digital controller uses a proportional-integral derivative (PID) to maintain the required setpoint temperature of the furnace. The main gases are argon (Ar) and acetylene (C_2H_2). The flowrates are monitored and controlled by a Brooks 5850E mass flow controller and Brooks 01545 Readout and Control Electronics indicator module. A flashback arrestor is mounted on the acetylene line due to the highly flammable and explosive nature of this gas. A schematic representation of the t-CVD setup is shown in Figure 3.1.

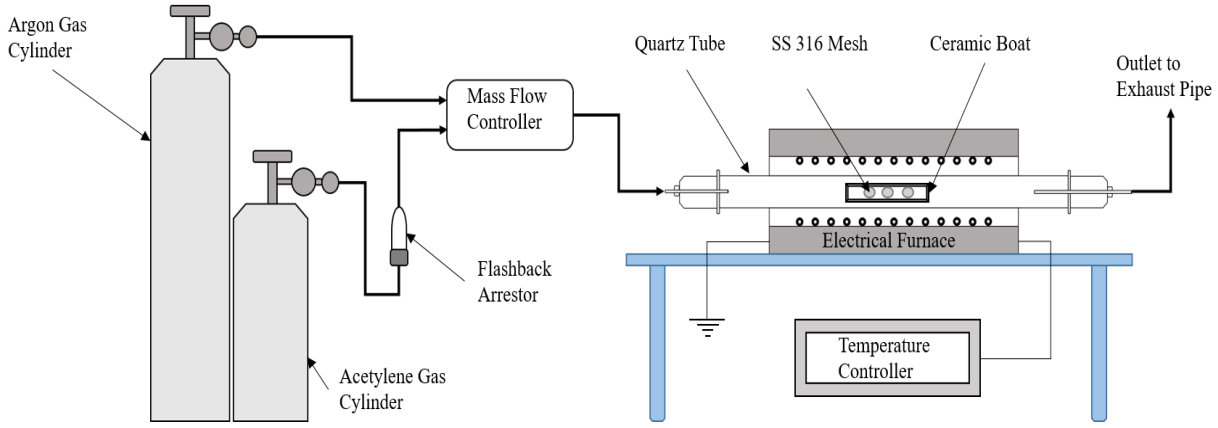

Figure 3.1-Schematic of thermal chemical vapor deposition setup

The MWCNT synthesis procedure is as follows. The samples, consisting of SS 316L, 400 series mesh with 25 μm grid bars are cut into 1.98 cm^2 circles using a 5/8-inch diameter hole punch. The mesh is then sonicated for 30 minutes in acetone in order to remove any grease or surface impurities. At this point the samples are weighed with an analytical balance. The sample will be weighed again after the MWCNT growth process to evaluate the mass of MWCNT produced. Each samples are then put in an alumina ceramic boat which is in turn placed at the center of the tube furnace. Both ends of the tube are sealed with quartz caps with a ceramic feeding tube. The inlet is linked to the mass flow controller while the outlet is discharged into a vented exhaust pipe. Argon is injected into the tube at 592±5 sccm. The furnace is then turned on to 700 ºC and the samples are heated for 30 minute under these conditions. After this heat treatment, acetylene is injected during four minutes at 68 ±5 sccm. This is followed by an isothermal growth period of 30 minutes in an Ar atmosphere, after which the system is allowed to cool down to room temperature.

3.1.2 Platinum Nanoparticles

To finalize the synthesis of the composite electrode used in this project, metal nanoparticles (NP) are added to the MWCNTs (i.e. anchored on MWCNTs). These particles are a central part of this process since they are responsible for the catalytic behavior of the composite electrode. The method used for the production of these nanoparticles is PLA. The time of nucleation and the size and composition of clusters depend on the type of material, the laser parameters, and the ambient medium. The parameters that are manipulated are the laser fluence and the total deposition time. The PLA technique supports fabrication of various nanomaterials with controlled size distribution

and different physical/chemical properties [31]. One of the advantages of using PLA is that it produces a narrow distribution of particles that can adhere to carbon nanotubes. Previous work has shown that the nanoparticles preferentially adhere onto MWCNT and that the macro-particles (diameter >1 μm), a usual co-product obtained with metal nanoparticles, are not collected [18]. According to the work of McArthur et al., NPs are formed under low pressure condition (mTorr or less), while films of the ablated material are deposited at a higher pressure (around 1 Torr) [1].

The PLA setup (Figure 3.2- Schematic of laser ablation setup (not to scale)Figure 3.2) in this project uses a pulsed Nd:YAG laser (Brilliant B10, Qunatel, France: 355 nm, 10 Hz, 5 ns). This laser delivers an incident bean at a wavelength of 1054 nm that goes through two harmonic generation steps which produce outputs of 532 and 355 nm respectively. The setup consists of two vacuum chambers separated with a pneumatic NW-100 gate valve. The first chamber serves as a loading site where samples can be quickly mounted to a circular stage attached to a linear displacement knob. This apparatus allows the sample to move to and from the second compartment. The second compartment is the ablation chamber where the target is mounted on a smaller stage attached to a stepper motor. This device moves the target up and down while keeping it in the path of the laser beam. The motion of the target prevents the beam from being focused on a single point thus preventing the beam from going through the target given its small thickness. The laser beam is reoriented and focused by a series of mirrors and lenses to hit the target at a 45º angle. A vacuum is maintained in both chambers using a rotary vane pump. The pressure in each chamber is monitored with separate piezoelectric pressure gauges. The same pump is used for both chambers; therefore, each chamber has an isolation valve so they can be operated independently. A photograph of the setup can be seen in Figure 3.3. A platinum target from the Kurt J. Lesker Company® with 99.99%purity was used.

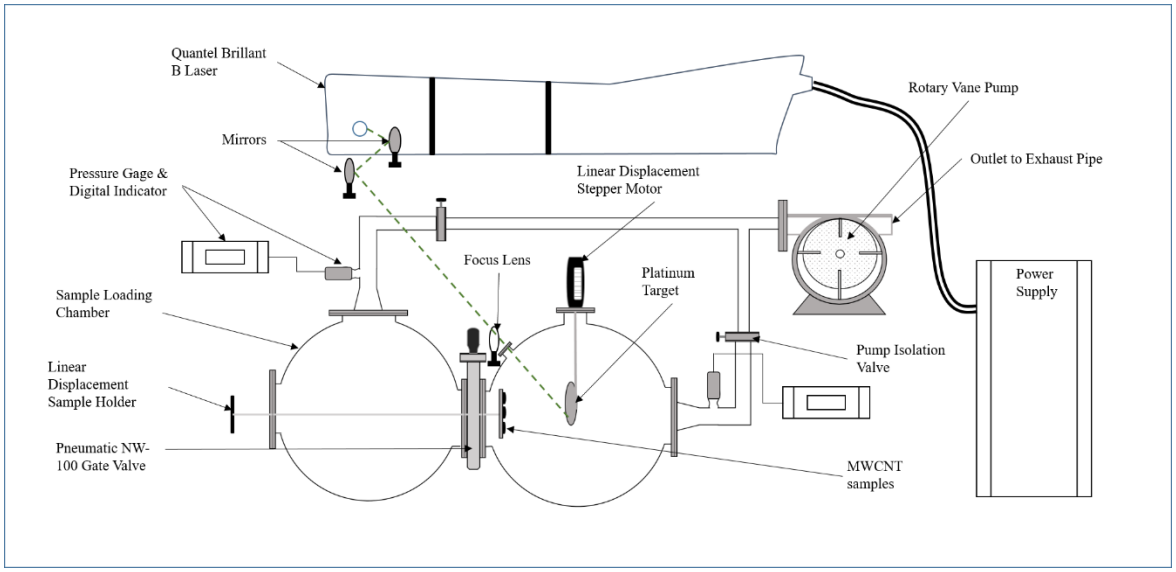

Figure 3.2- Schematic of laser ablation setup (not to scale)

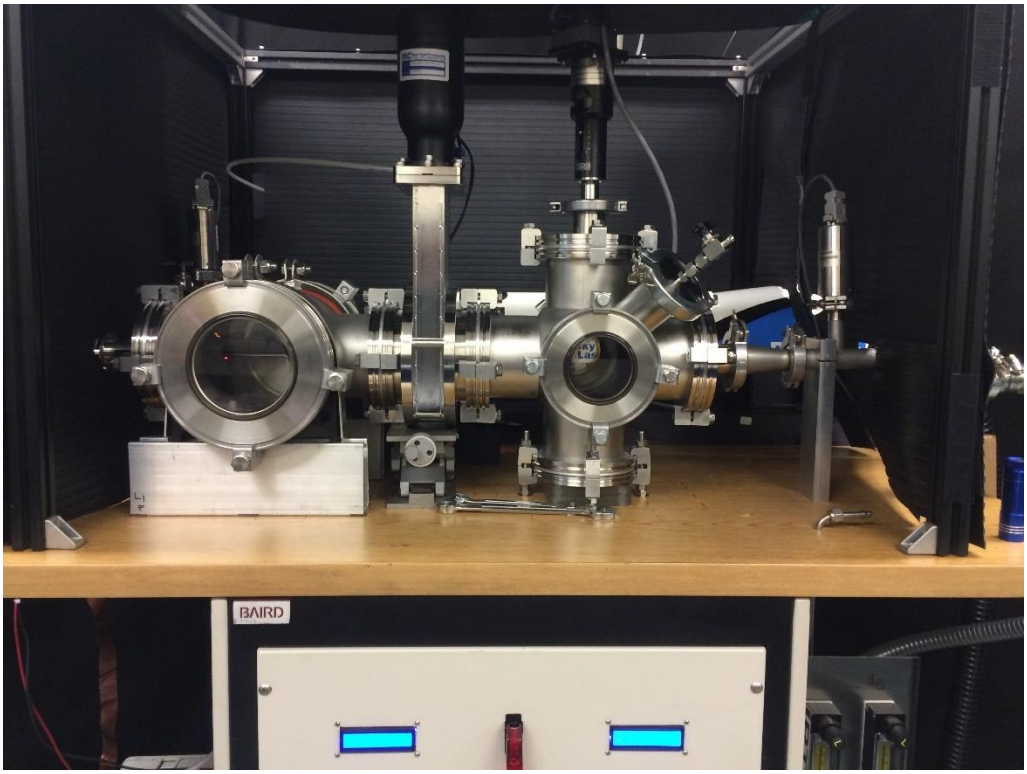

Figure 3.3-Photograph of laser ablation setup

The procedure used for the deposition of nanoparticles is as follows. The loading chamber is isolated from the pump by closing the isolation valve and the gate valve. The chamber is allowed to repressurize to atmospheric pressure. The previously weighted MWCNT-covered SS samples are mounted on the sample holder, and then the chamber is sealed. Following this step, the metal target is polished with rough sandpaper to remove any impurities. It is then sonicated for 30 minutes in acetone. The loading chamber is isolated and repressurized similarly to the loading chamber: the target is mounted to the small stage and the chamber is sealed, then the isolation valves are opened and air is pumped out of the chambers for several hours until they reach the base pressure of 4 mTorr. The gate valve is opened and the stage on which the samples are mounted is positioned 7 cm from the target. At this point the power supply of the laser is turned on. The flashlamp/Q- switch delay is set to an optimum of 215 μs so that the laser operates at a very high energy (fluence of 2.36±0.01 $J.cm^{-2}$). The stepper motor is turned on and a plasma plume forms at the surface of the target, indicating that ablation is taking place. The following ablation times were used: 2.5 min; 5 min; 10 min; 20 min; 30 min; 40 min.

3.2 Electrochemical Testing Cell

The electrochemical activity of the composite electrodes was analyzed using a standard three-electrode cell depicted in Figure 3.4. The counter electrode (CE) used was a graphite rod separated from the other electrodes by a glass frit. The glass frit prevents the diffusion of O_2 into the main compartment so as to prevent interference in the HER. This is done by the use of a glass filter obtained from Ace Glass with a pore diameter ranging from 25 to 50 μ (Ace Glass, Porosity C). The working electrode (WE) is mounted into a plastic Teflon holder which exposes a geometric area of 0.785 cm^2 of the composite electrode to the electrolyte solution. The reference electrode (RE) used for all electrochemical measurements is a saturated calomel electrode (SCE; E=0.241 V vs standard hydrogen electrode (SHE)). The instrument used for electrochemical analysis is a Metrohm Autolab PGSTAT 30. This modular potentiostat/galvanostat, with a compliance voltage of 30 V and a bandwidth of 1 MHz, combined with our FRA32M module, is specially designed for electrochemical impedance spectroscopy. The instrument was operated using NOVA 2.0 software.

Electrochemical testing was carried out in both acid (0.5M H_2SO_4) and alkaline (1M NaOH) conditions. The WE potential window used in acidic conditions ranged from -0.9 to -0.2

V (vs SCE) and in the alkaline solution -1.6 to -0.95 V (vs SCE); in terms of the HER overpotential, this corresponds to a range of -0.67 to 0.03 V in acidic condition. In alkaline condition the corresponding overpotential is from -0.57 to 0.08 V. The electrolyte was purged with argon for 40 minutes prior to any measurements.

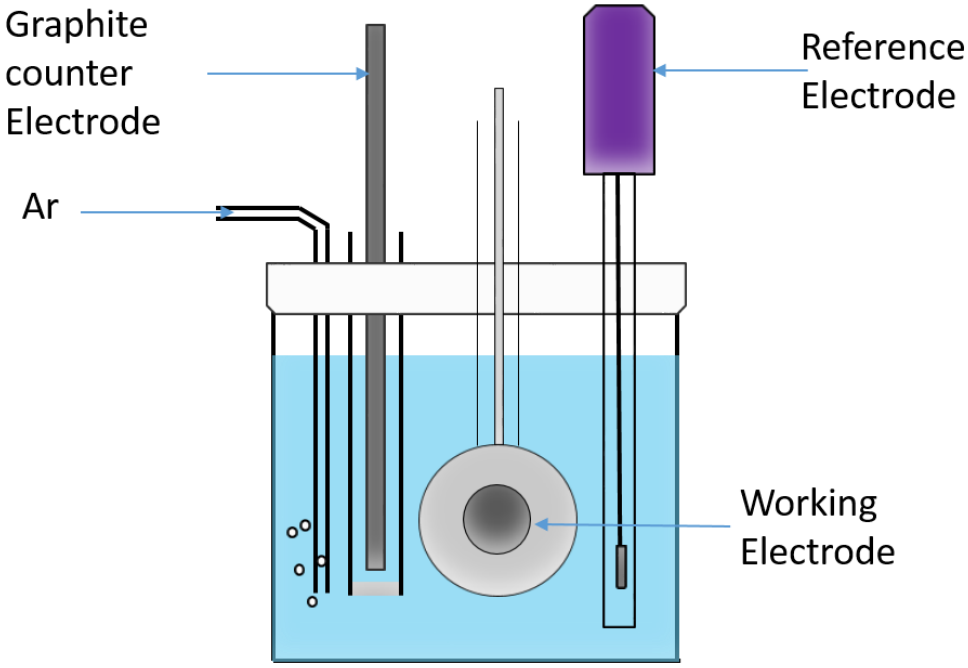

Figure 3.4-Schematic of a three-electrode electrochemical cell used for characterization on composite electrodes

3.3 Characterization Techniques

3.3.1 Electron Microscopy

Electron microscopy was used to characterize the morphology of the Pt NP-MWCNT cathodes. A filed-emission scanning electron microscope (FE-SEM; Hitachi SU-3500) uses electron beams to scan the surface of a sample. The electron beam irradiates the sample and produces a signal which can be analyzed for surface morphology and topography. The sample must be conductive to avoid charging effects which can blur the image [36]. As the electrons strike the surface, they penetrate the surface and collide with surface atoms, creating a region of excitation. These excitations can be secondary electrons, backscattered electrons, and certain X-rays [36]. Secondary electrons produced from inelastic surface scattering reach a detector in

greater numbers and this can be used to generate topographic information. This instrument was mainly used for the characterization of the MWCNT morphology.

Transmission electron microscopy was used to characterize in more detail the various concentric nanotubes and platinum nanoparticles deposited on the MWCNTs (TEM; Phillips CM200). In addition, the electron diffusion spectroscopy module on the instrument was used to identify platinum on the MWCNTs and perform electron diffraction measurements. Much like SEM, TEM uses a highly focused electron beam. In the case of TEM, the beam is applied to a very thin sample as electrons must pass through it. Those electrons then travel through an imaging detection system and the image is then displayed. Unlike SEM, TEM analysis is two-dimensional, which makes it ideal for examining crystalline structures.

3.3.2 Linear Tafel Polarization

Linear Tafel polarization (LTP) is a linear sweep voltammetry (LSV) technique in which the results are presented in a semi-log plot. LTP was used to determine the activity of produced electrodes and the kinetic parameters (Tafel slope, exchange current density). LSV involves sweeping the electrode potential between limits E_1 and E_2 at a known sweep rate, v ($V.s^{-1}$), before halting the potential sweep. The current is measured and plotted on a logarithmic scale, according to the Tafel equation presented earlier in the thesis (Equation (20)). For the analysis of the activity on the composite electrode, a slow scan rate of 1 $mV.s^{-1}$ was used. In order to study the HER LTP, measurements must be carried out in the potential regions negative of the reversible hydrogen potential (η=0). Consequently, the actual potential applied will vary depending on the reference electrode being used and the pH of the electrolyte as predicted by the Nernst equation. The results of the sweep (i vs η) are plotted on a semi-logarithmic scale to yield a Tafel plot. The inverse of the slope yields the Tafel slope.

3.3.3 Chronopotentiometry

Chronopotentiometry is a technique in which the current is controlled (kept constant) while measuring potential. This technique can be used to measure capacitance, life cycle, energy density, maximal voltage, power density and the Equivalent Series Resistance. The technique measures the potential over time as the device charges/discharges. In this project it was used in its simplest form to assess the stability of the Pt NP-MWCNT cathodes over time. A constant current density

of 200 $mA.cm^{-2}$ was applied to the electrode over cycles of 24 hours. During this period the potential was sampled and recorded every second.

4 Results and Discussion

The following section presents the results of the experimental work done in this thesis. All results are presented and discussed simultaneously. The results are divided in three major sections. The first section is the physical characterization of the working electrode. This section includes a characterization of the general morphology of the electrode along the various steps of its production. Then, the morphology and the size distribution of platinum of the surface is presented. Finally, the mass density of platinum on the electrodes is presented. The second section investigates the catalytic activity of the electrodes for the HER through the presentation and discussion of electrochemical data. Results are discussed first for data obtained in an acidic electrolyte then in an alkaline electrolyte. Finally, electrochemical testing is used to the determine the stability of the electrode during operation.

4.1 Physical Characterization

4.1.1 Electrode Morphology

Figure 4.1shows the general morphology of the composite electrode when observed through electron microscopy. Figure 4.1-A shows the morphology of the stainless steel mesh before the MWCNT growth process. Figure 4.1-B is a low-resolution SEM image of the MWCNT-Pt nanoparticle electrodes. The carbon nanotubes present on the electrode form a dense network of intertwined tubes. Although the tubes form a dense Velcro-like assembly, there remains a large amount of open space for electrolyte penetration, thus creating a large 3-dimensional (3D) surface area. Platinum nanoparticles were deposited for 10 minutes on this electrode. However, the particles cannot be seen at such low magnification. Figure 4.1-C shows a high-resolution TEM image of bare MWCNTs. The nominal diameter of the tubes ranges from 30 to 120 nm. The tubes are for the most part hollow with a smooth surface. At some discrete locations some rather large particles seem to be imbedded inside the tubes. Also, this image confirms the multiwall nature of the carbon nanotubes, as the concentric border of the tubes can be seen in this image. Figure 4.1-D shows MWCNTs after 10 minutes of PLA. Unlike the bare MWCNTs, these tubes have dotted

spots which are assumed to be platinum nanoparticles. The particles vary in size, although they are all in the nanometer range. They are well dispersed along the surface of the tubes.

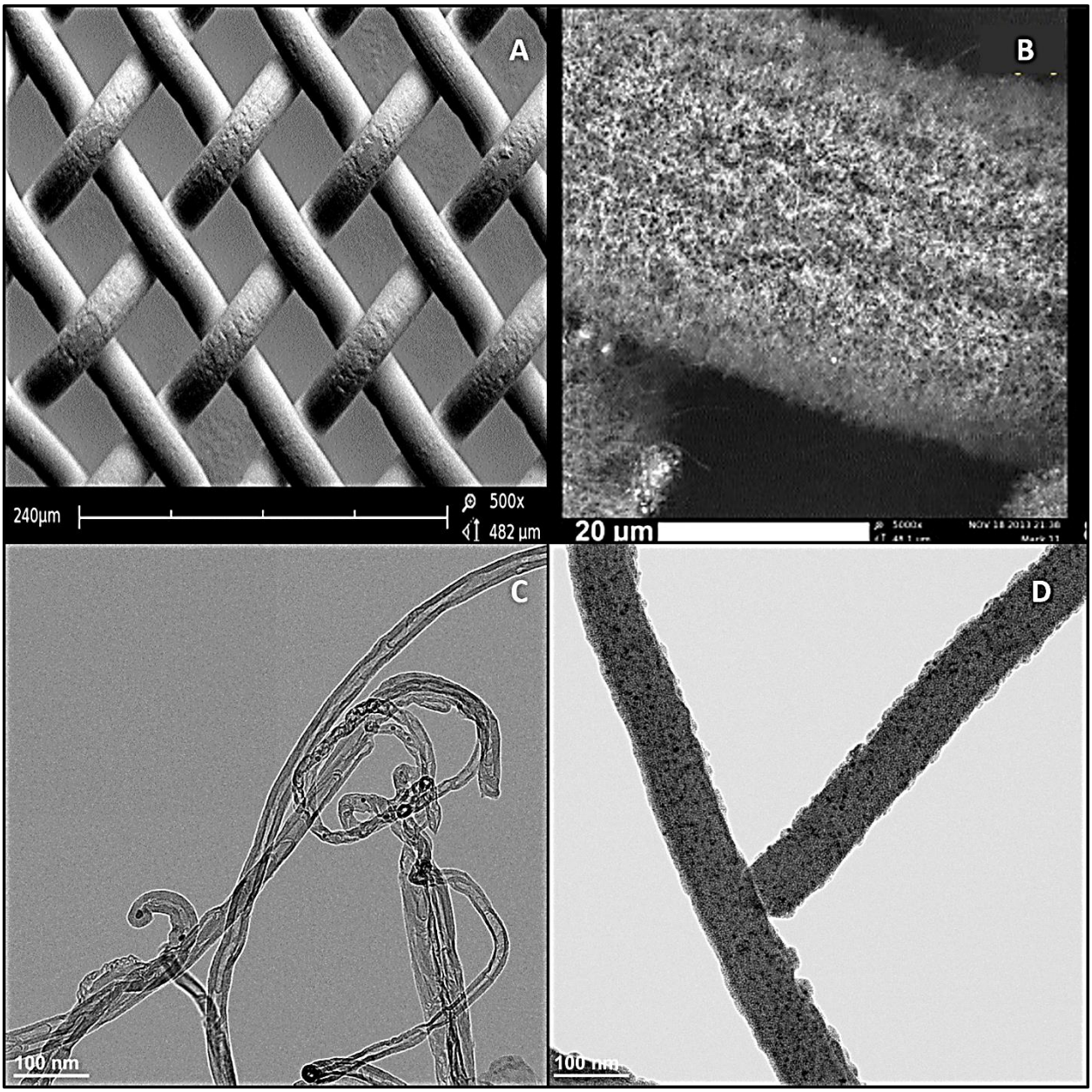

Figure 4.1-Morphology of the electrode along the production process. A) Bare stainless steel mesh. B) Mesh covered with Pt NP-MWCNTs. C) Bare MWCNTs. D) MWCNT covered with Pt nanoparticles

The large particles present in the bare MWCNT may be iron islands from the stainless steel substrate. These particles act as catalytic sites for the synthesis of the tubes. This theory is supported by the fact that these particles span exactly the radius of the tube in which they are imbedded. The presence of the iron particles in the middle section of the tube may be indicative of a mixed growth mechanism. The detailed study of the growth mechanism of the tubes is beyond the scope of this project. EDX results in Figure 4.2 show that the particles observed in Figure 4.1-D are made of platinum. Platinum was only present in samples that had gone through PLA, unlike Fe, Cr, and Ni, which are always present. These elements originate from the SS mesh used as substrate for the MWCNT growth. The presence of well-dispersed particles throughout the length of the CNTs indicates, firstly, that PLA is a good method for producing non-agglomerated individual particles. Secondly, it shows that the particles can penetrate the network of CNT to be deposited throughout the tube array, thus taking full advantage of the high surface area offered by the carbon nanotubes.

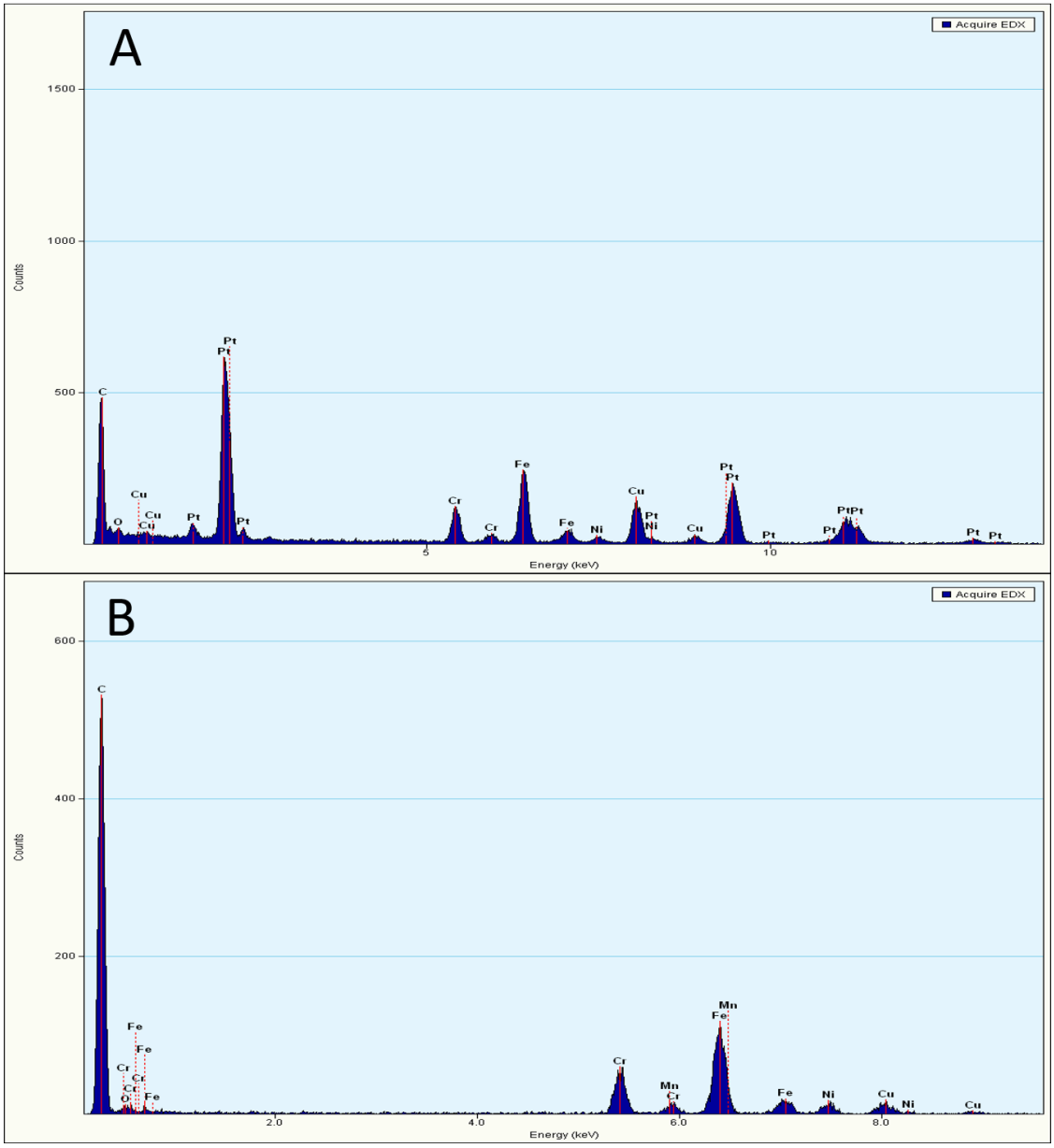

Figure 4.2-EDS analysis of: A) MWCNT after 10 min of PLA; B) Bare MWCNT

4.1.2 Morphology of Platinum on MWCNT

Figure 4.3 and Figure 4.4 show the morphology of platinum on the MWCNT at deposition times of 2.5, 10, 20, and 40 minutes. Figure 4.3 shows the bright field images while Figure 4.4 shows the same images in a dark field. In Figure 4.3-A and Figure 4.4-A the particles produced after 2.5 minutes are shown. They are best seen in the dark field image.The particles are very small

and well dispersed. They do not affect the general morphology of the tubes wich remain smooth. Figure 4.3-B and Figure 4.4-B show MWCNT after a PLA time of 10 minutes. The dark field image shows a greater particle density on the MWCNT, which is expected. However, the bright field image reveals some changes in the surface morphology of the MWCNTs. The previuosly smooth MWCNT surface has some irregularities in the form of grooves and bumps. In Figure 4.3-C and Figure 4.4-C, MWCNTs are shown on which platinum nanoparticles have been deposited during 20 minutes. In the dark field image, just a few particles can be seen, with some much larger than in the previous images. When observed in bright field, the surface of the MWCNTs is radically different. It is covered by an uneven layer of platinum nanoparticles that forms bumps and grooves. Finally, Figure 4.3-D and Figure 4.4-D show the morphology of MWCNT after 40 minutes of PLA. The dark field image shows no partticles on the surface of the MWCNTs. Instead, the bright field image reveals the formation of a layer of platinum which completely covers that MWCNT with, in addition, large drop-shaped agglomarates all over the surface.

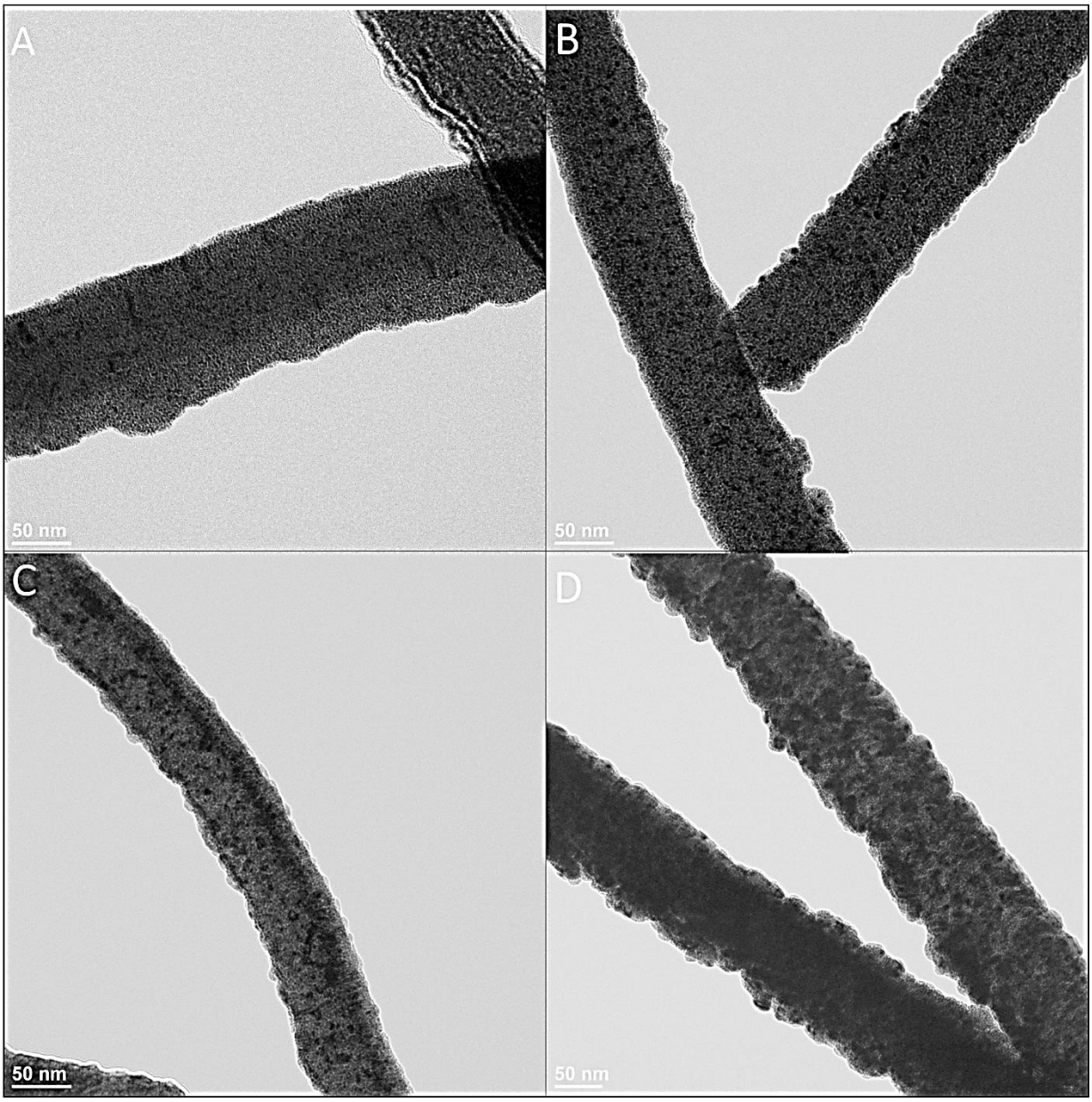

Figure 4.3-TEM images showing the morphology of PLA deposited platinum on MWCNTs. A. Deposition time of 2.5 minutes; B. Deposition time of 10 minutes; C. Deposition time of 20 minutes; D. Deposition time of 40 minutes

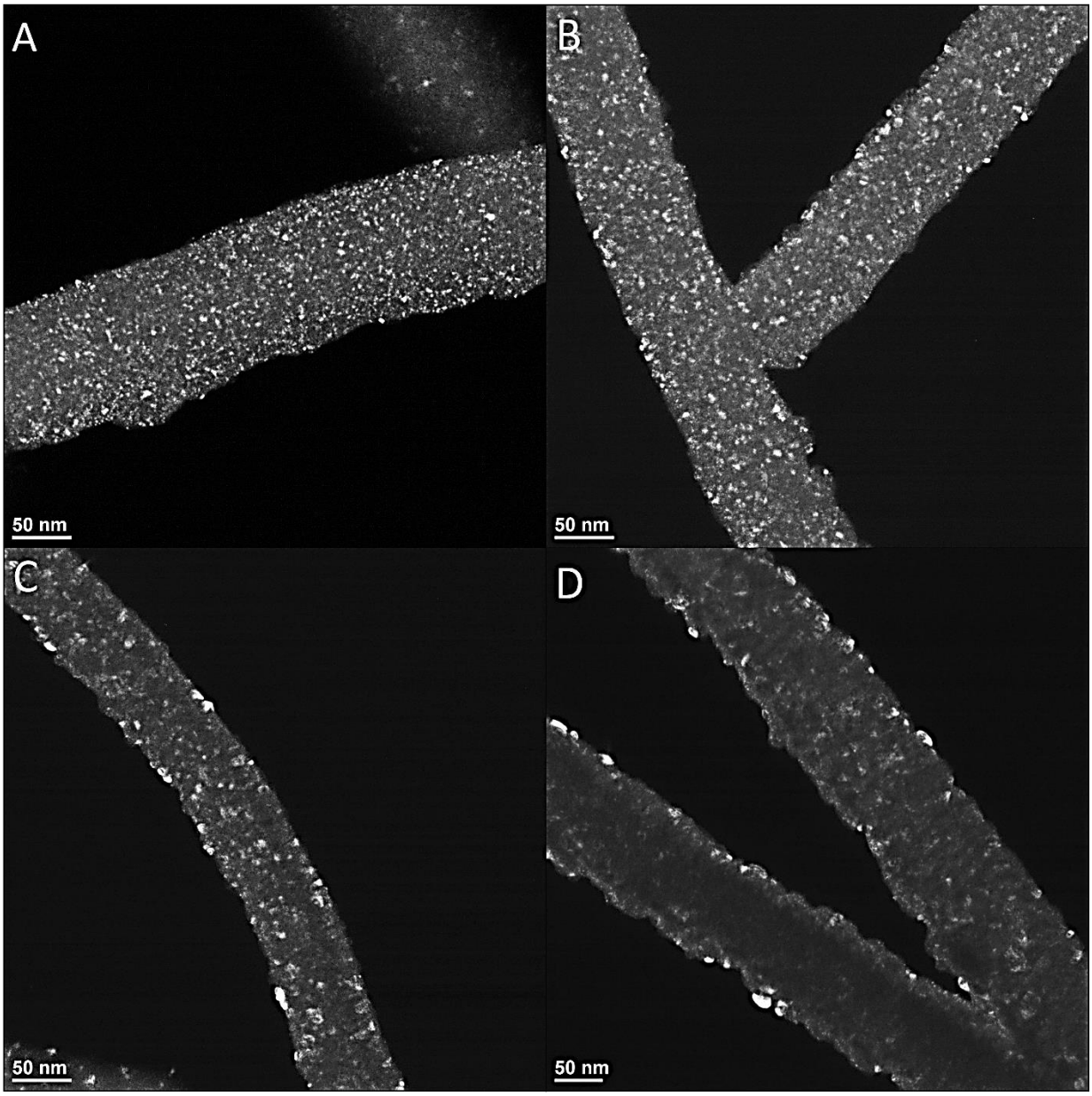

Figure 4.4-Dark field TEM images showing the morphology of PLA deposited platinum nanoparticles on MWCNTs. A. Deposition time of 2.5 min; B. Deposition time of 10 min; C. Deposition time of 20 min; D. Deposition time of 40 min

From the analysis of the morphology of the Pt NP-MWCNTs composite electrode produced with various deposition times, it can be said that the deposition time greatly affects the coating morphology on the MWCNTs. At low deposition times (i.e. lower than 10 min), well-dispersed individual particles are deposited onto the surface. At higher deposition times, the particles eventually cover the entire surface of the MWCNTS to form a wave-like layer of platinum

nanoparticles. As deposition time is further increased, large particle agglomerates form on top of the layer of platinum. The surface of the MWCNT prevents the agglomeration of platinum once deposited on the surface. The surface area of collection and also, the surface forces acting between the MWCNT and the metal nanoparticles aid towards preventing nanoparticle agglomeration as observed by Rao et al. However, when the surface is completely covered, additional particle deposited are free to agglomerate. This observation corroborates the idea that the MWCNTs act as ideal particle collectors mainly for small nanoparticles and prevent their agglomeration.

4.1.3 Particle Size Distribution

Figure 4.5-B and Figure 4.6-B show the Pt nanoparticle size distribution for PLA times of 2.5 and 10 min, respectively. The particle size distribution was obtained through a Matlab® algorithm written to identify and determine the diameter of nanoparticles based on the contrast between the nanoparticles and the surface of MWCNTs in dark field images obtained from TEM. The particles' size follows a log-normal distribution, as can be seen from the fitted log-normal curve in Figure 4.5-B and Figure 4.6-B. The log- normal mean and variance are also presented in Figure 4.5-B and Figure 4.6-B. The distributions are relatively narrow. Furthermore, the average particle size of 3.6 nm is a desirable feature of PLA, since smaller particles will maximize the electrochemically active surface area and the catalytic activity of platinum.

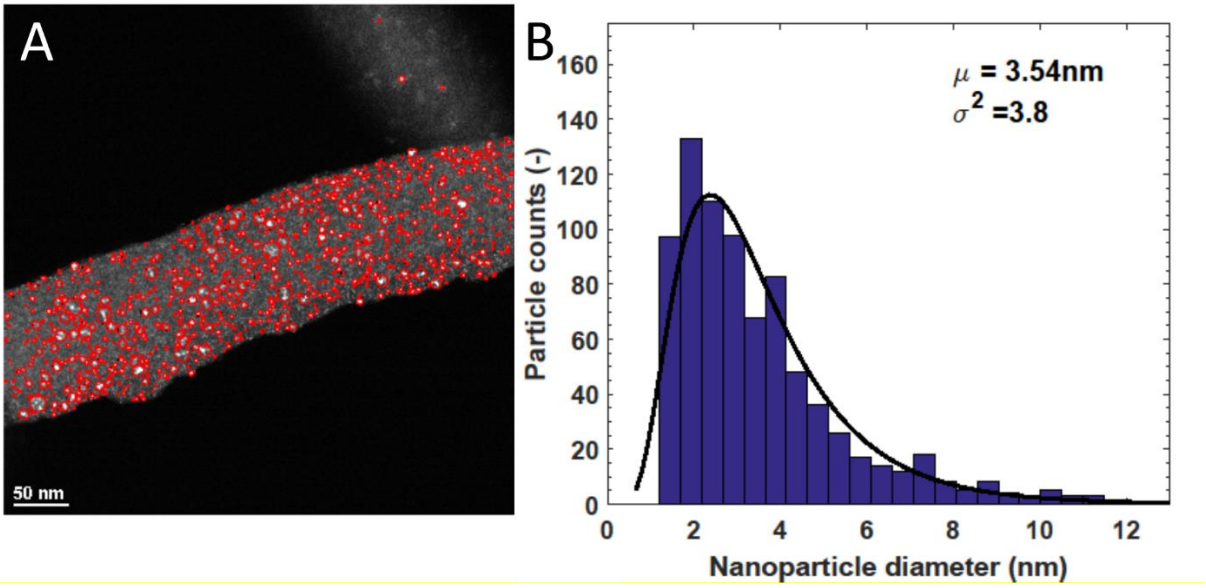

Figure 4.5-Platinum nanoparticle size distribution with a deposition time of 2.5 minutes

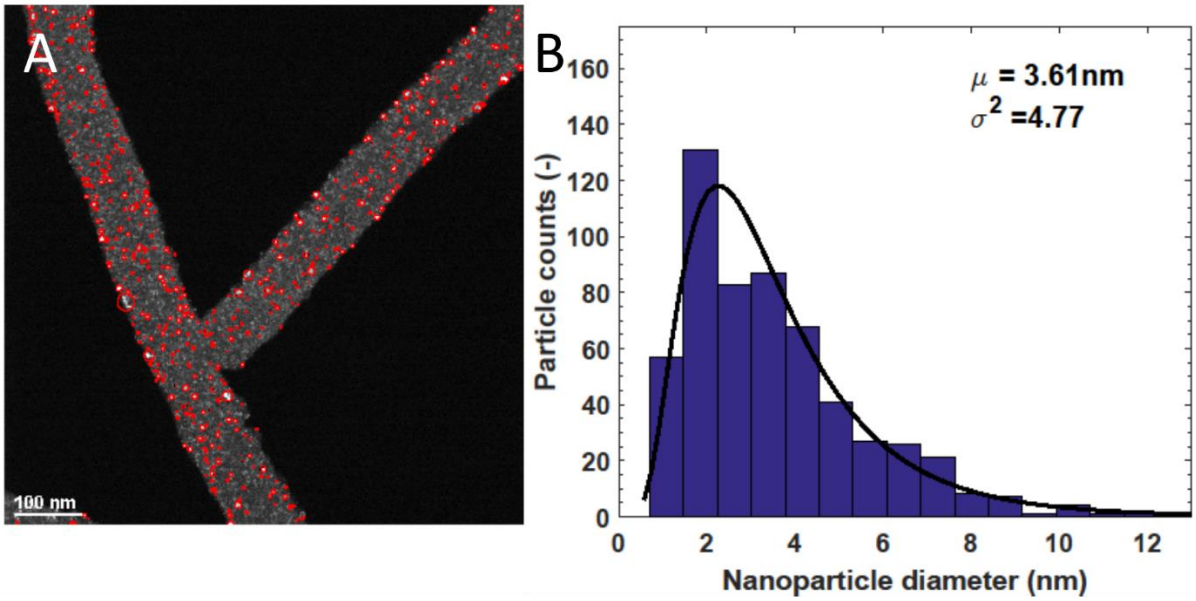

Figure 4.6-Platinum nanoparticle size distribution with a deposition time of 10 minutes

The log-normal mean in both cases is not significantly different based on a t-test that show a p-value of 0.084. Therefore, it can be inferred that deposition time does not affect the size of the particles. This observation is expected, since it was mentioned previously that the distribution of particles is mostly a function of the cooling rate, which is in turn controlled by pressure and temperatures (i.e. temperature of the expending plume interacting with the background gas in the chamber) in the chamber. Since all depositions were done at a base pressure of 4 mTorr, it is expected that the particles remained small for all deposition times. The low pressure used in this deposition process enhances the cooling rate and reduces the number of atoms colliding to produce the particles, thus allowing the nanoparticles to form in flight prior to their attachment to the MWCNT substrate. In addition, the lack of agglomeration on the surface corroborates the idea that nucleation and growth of the particles occur in flight rather than on the surface. However, the total surface coverage increases very rapidly with the deposition time due to the high fluence at which the laser is operated. As a consequence, at high deposition times individual nanoparticles can no longer be distinguished from the layer of platinum that covers the entire surface of the MWCNTs. At this point particles start to pile on and form a granular coating. However, a large number of nanoparticles can be deposited before a granular coating is obtained.

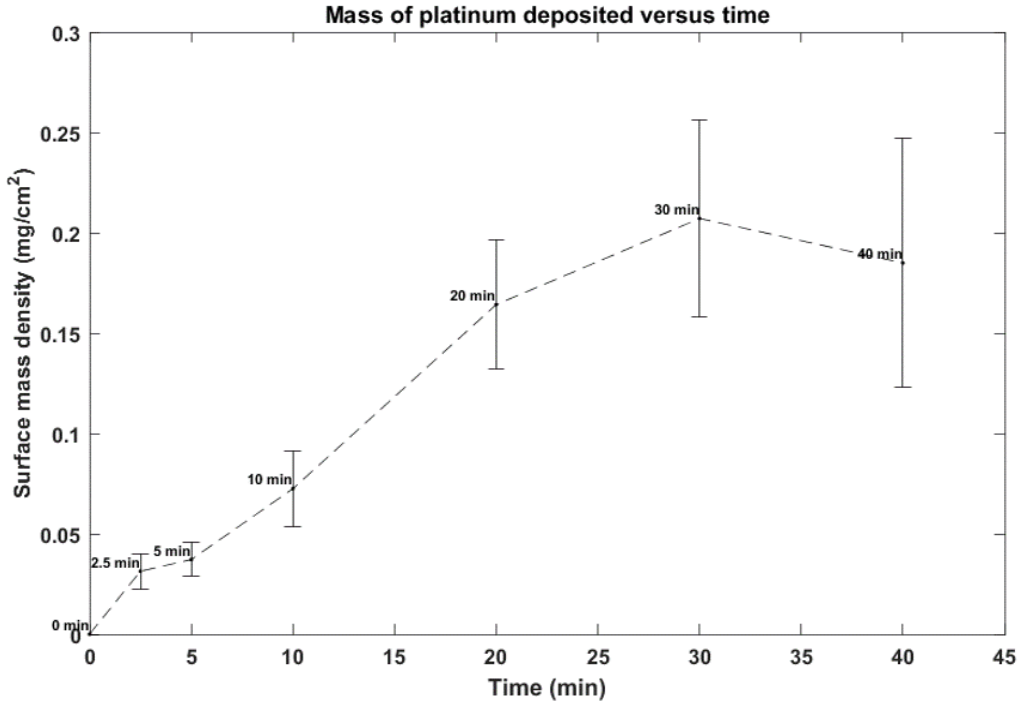

Figure 4.7-Surface mass density of platinum nanoparticles deposited as a function of ablation time

Figure 4.7 shows the mass of platinum nanoparticles deposited per unit geometric area for various deposition times. The mass was determined by weighing the sample before and after PLA. As it can be seen in this figure, the mass loading increases sharply from 0 to 2.5 min. Then, the mass loading increases at a slower rate quasi-linearly from 2.5 to 20 min. From 20 to 30 min the loading continues its increase at even a lower rate. Finally, from 30 to 40 min the loading decreases very slightly. However, it should be noted that there is no actual statistical difference between the loadings achieved between 30 and 40 min (with a p-value of 0.2).

Firstly, it must be noted that very low loading can be achieved using PLA. For deposition times below 5 minutes the loading is always below 0.05 mg.cm^{-2}. This value is almost two orders of magnitude lower than the quoted 1 mg.cm^{-2} used in commercial electrolyzes [37]. The loading quoted in literature spanned a wide range of 0.014 to 18 mg.cm^{-2} [11, 38, 39]. In our experiments the lowest loading (0.0252 mg.cm^{-2}) was achieved with a deposition time of 2.5 min. Although it has not been done in the current work, the deposition time can be further reduced. In addition, experiments not presented here have shown that PLA on platinum can be done at lower fluence.

Therefore, lower loadings can be achieved and should be considered for future work. The quasi-linear increase in loading observed from 0 to 20 minutes is attributed to the increase in nanoparticle coverage of the MWCNT surface. The increase in mass at higher deposition times that occurs at a much slower rate can be explained by the following scenarios. As complete coverage of the surface is achieved, the incoming nanoparticles do not adhere as well to the granular coating or some parts of the coating flake off. The small decrease observed between 30 and 40 minutes is not significant enough to indicate that material is lost at 40 minutes, due to the large variability in the sample deposited at those times.

4.2 Electrochemical Characterization

4.2.1 Tafel Plot in Acidic Conditions

Figure 4.8 shows the Tafel curves for various cathodes in the hydrogen evolution region. The current density is normalized with respect to the geometric area of the electrode. Curve (a) shows the response for a pure platinum wire, (b) a bare MWCNT, (c) a MWCNT with platinum deposited using PLA during 2.5 min, (d) 5 min, (e) 10 min, (f) 20 min, (g) 30min. As mention in the theoretical section, the current density represents the catalytic activity of the cathodes (i.e. the amount of H_2 produced), while overpotential is the driving force for electron transfer in the hydrogen evolution reaction (HER) (i.e. the energy input). Therefore, an ideal catalyst would exhibit a high current density at a low overpotential.

Curve (a) in Figure 4.8 shows that pure platinum has lower current density than the Pt NP-MWCNT composite electrodes at all overpotentials. At the other end, the bare MWCNT curve (b) has the lowest catalytic activity, as it is lower by two orders of magnitude than any Pt NP-MWCNT composite electrode. The following three curves, (c), (d), (e), are very close to each other. Although these curves have different Pt loading, they do not seem to differ significantly. However, these curves are two orders of magnitude higher than the Tafel curve of bare MWCNT, thus showing their superior catalytic properties towards the HER. Curve (f) which has a higher PLA of 20 min is above the previously mentioned group. Finally, curve (g), which has the highest PLA deposition time of 40 minutes, has the highest catalytic activity among the composite electrodes.

Firstly, the low catalytic activity of the bare MWCNT electrode is not surprising, since carbon bases materials are known to have very large overpotential for the HER. Therefore, it is expected that MWCNTs have low catalytic activity in the potential region investigated. Also, it

must be noted that the addition of platinum significantly increases the catalytic activity of the composite electrode as opposed to the bare MWCNT. Therefore, the platinum deposited via PLA is catalytically active. Secondly, curves (c) and (d) represent the catalytic activity of two cathodes that have very close mass loading. Therefore, it is not very surprising to observe that these curves are very close to each other. However, curve (e), which represents the current density of the cathode with 10 min PLA time, has a loading quite different statistically from that of the cathodes with PLA times of 2.5 min and 5 min, as noted in Figure 4.7. Nevertheless, as stated before, curve (e) does not differ significantly from (c) and (d). This may be explained by variability in the data, which will be addressed shortly in the analysis of Figure 4.9. Another possible explanation is that at such low mass loading the increase in platinum coverage is not significant enough to make a difference in the overall catalytic activity of the electrode or the actual increase in Pt loading does not produce the proportional increase in surface area of Pt exposed to the electrolyte; therefore, the current density does not vary by much. Finally, and most importantly, it must be noted that all composite electrodes have a higher current density at the measured overpotential in comparison to the MWCNT and pure Pt-wire electrode.

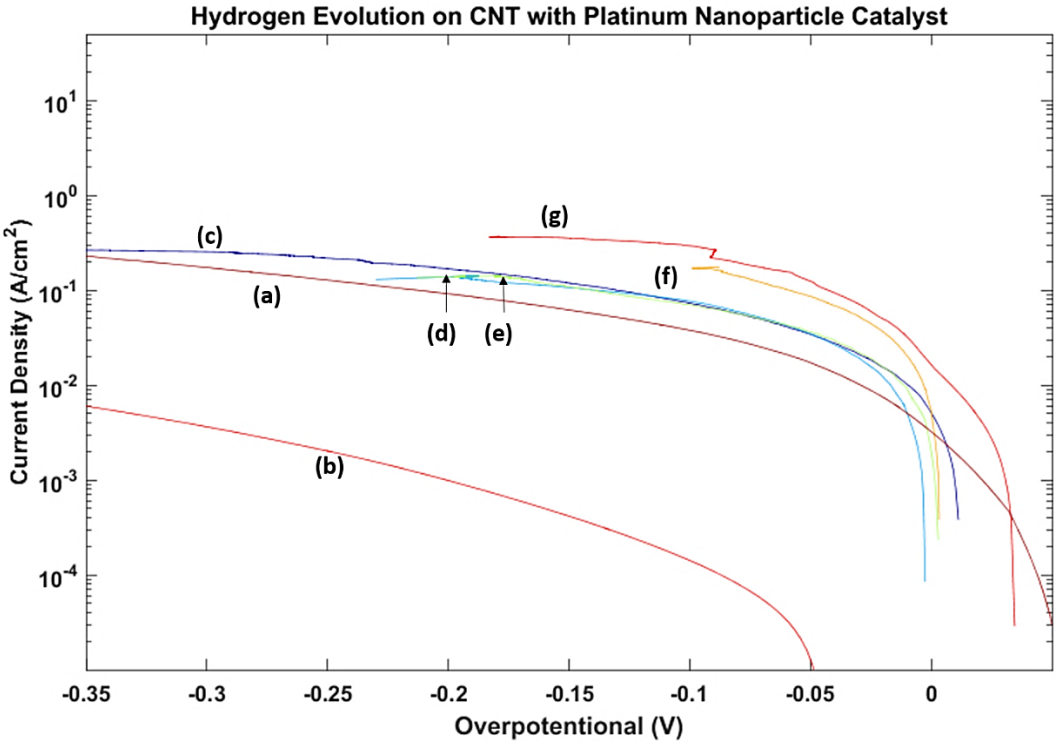

Figure 4.8-Tafel plot: Current density as a function of overpotential for various electrodes in 0.5 M H2SO4. (a) Platinum wire, (b) Bare MWCNT, (c) 2 min 30s Pt NP-MWCNT, (d) 5 min Pt NP-MWCNT, (e) 10 min Pt NP-MWCNT, (f) 20 min Pt NP-MWCNT, (g) 30 min Pt NP-MWCNT.

In order to address the variability in the current-overpotential curves and quantify the electrochemical activity of the cathodes presented in Figure 4.8, it is useful to examine the current density at a specific overpotential. This allows for statistical treatment of replicated measurements done for each composite electrode (not shown in Figure 4.8). The resulting analysis is shown in Figure 4.9. This figure shows the average current density for the various Pt NP-MWCNT electrodes mentioned previously as a function of depositing time. All current densities were determined at an overpotential of -90 mV. Figure 4.9 shows that the mean electrocatalytic activity of the cathodes increases steadily with the PLA time. However, the large variation observed in the activity of the Pt NP-MWCNT cathodes with deposition times of 2.5 min, 5min, and 10 min suggest that the differences may not be statistically significant, due to the large error present. The large error observed may be attributed to the variation in mass loading for the same deposition times. The continued increase observed at higher deposition times of 20 min and 30 min suggests

that the additional platinum added to the MWCNT increase the electrocatalytic activity of the composite electrode due to the Pt electrode coverage increase (area of Pt exposed to the electrolyte). As mentioned in the previous section, the platinum penetrates deep into the MWCNT forest instead of forming a layer only on top of the MWCNTs. Therefore, even when the MWCNTs are completely covered the full 3D support of MWCNTs offers a very large area for catalyst exposed to the electrolyte. After complete converge is achieved, the platinum structures that bulge out of the MWCNT, as seen in Figure 4.3-D, continue to increase the platinum area available for the HER to proceed. Furthermore, the higher catalytic activity observed in the composite cathodes relative to the pure Pt wire (Figure 4.8) is possibly due to the normalization with respect to the geometric area that was done for the Pt NP-MWCNT. The actual electrochemically active area of the Pt NP-MWCNT electrodes is much larger than the geometric area; therefore, there are many more catalytic sites that are being accounted for with this sample normalization. Attempts have been made to determine the true electrocatalytically active area of the composite electrodes, but without success.

In Figure 4.10 the same data as in Figure 4.9 is presented. However, the current density is now normalized with respect to the mass of platinum added. The current density can be assumed to stay constant despite the variability observed in replicate measurements. This indicates that activity of platinum remain unchanged with deposition time. This confirms that the increase in activity observed in the previous section is due to an increase in the MWCNT coverage by platinum, i.e. to the increase in surface area of Pt exposed to the electrolyte, and thus to the increase in surface area available to the HER. There does not seem to be any synergistic affect between MWCNTs and Pt at play.

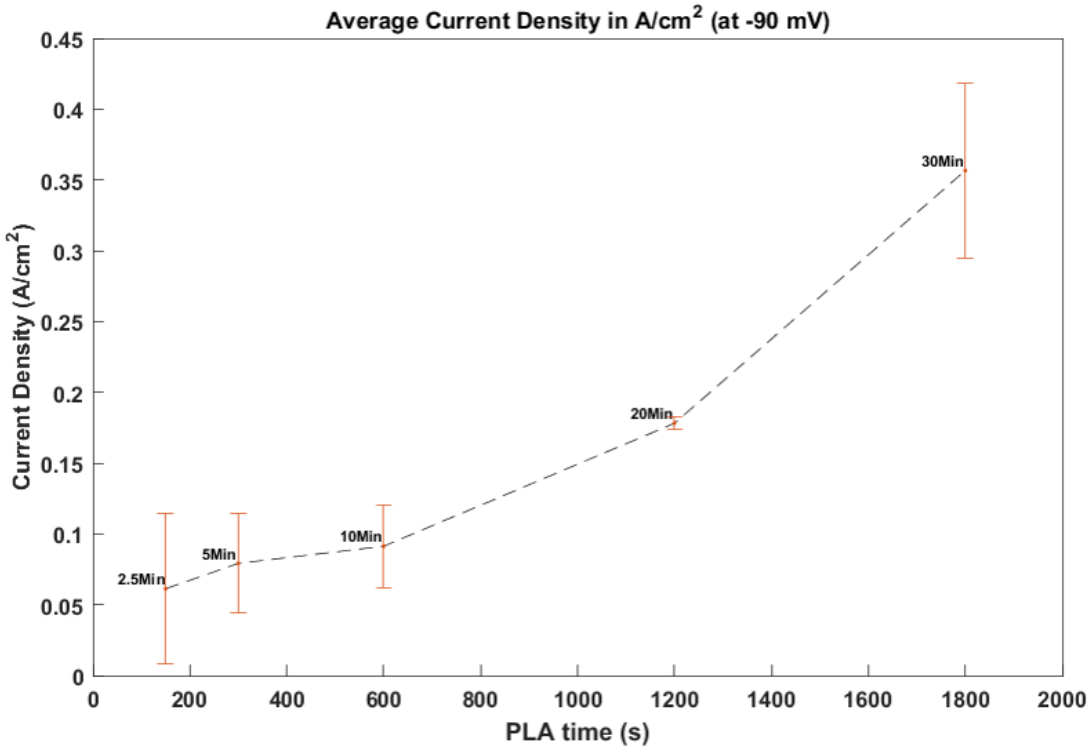

Figure 4.9- Current density normalized by unit geometric area, for various composite electrodes as a function of PLA time (measured in 0.5M H2SO4)

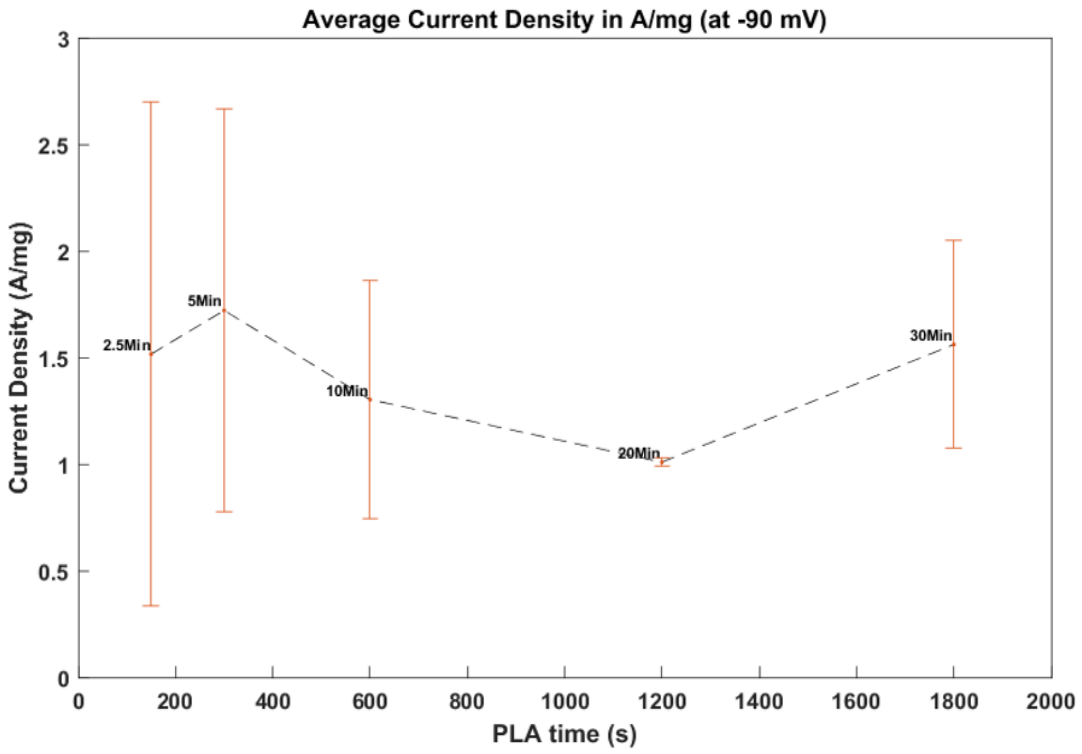

Figure 4.10-Current density normalized by mass of platinum for various composite electrodes as a function of PLA time (measured in 0.5M H_2SO_4)

The Tafel plot in Figure 4.8 also provided other relevant information on the catalytic and kinetic activity of the composite cathodes. The three parameters extracted from this plot are the Tafel slope b_C (mV.dec^{-1}), and the exchange current density. These parameters are presented in Table 1. In addition, the current density for each composite electrode is show at the chosen potential of 90 mV. The first parameter presented is the Tafel slope. It has been shown that this parameter yields information on the limiting step in the mechanism involved in the HER, as discussed before in the thesis. The mechanism of the HER on platinum in acid electrolyte has been studied extensively by Bockris et al. [15]. The Tafel slope observed for the composite electrodes with deposition times of 2.5, 5min, 10 min and the Pt wire is consistent with the slope of 30 mV.dec^{-1}reported in literature. In addition, the exchange current density for the composite cathodes, which ranges from 5 to 6 mA.cm^{-2}, is very close to the typical 1 mA.cm^{-2} value reported. These parameters suggest that the reaction mechanism follows the Volmer-Tafel routes (Equations (23) -(24)) with the Tafel step acting as the rate-determining step. This step involves the reaction of two adsorbed hydrogen atoms on the surface of the platinum to form hydrogen gas (Equation

(24)). The higher exchange current density is an indication of the slightly higher catalytic activity of the composite electrode with respect to the bulk platinum. The remaining two cathodes (20 and 30 min in Table 1) had higher Tafel slope values. Bockris et al. demonstrated that the presence of impurities on the platinum electrode may cause a change in the mechanism. In that case, a Tafel slope of 58 $mV.dec^{-1}$was obtained. The introduction of impurities caused the diffusion of adsorbed hydrogen on the surface to be more sluggish. In our case, impurities may have been introduced to the cathode during the nanoparticle deposition process. PLA does not usually cause the addition of impurities on the MWCNT as long as the material being ablated is not contaminated. However, in our case, the platinum target was very thin, and on occasion during the long depositions the laser beam pierced the target, thus causing ablation of the steel support in small quantities. The Tafel slopes in these last two electrodes (20 and 30 min in Table 1) are closest to the theoretical Tafel slope of 40 $mV.dec^{-1}$. Consequently, it can be inferred that the reaction follows the Volmer-Heyrovsky routes, but instead of having the Heyrovsky step as an RDS, the slow surface-diffusion of adsorbed hydrogen is the RDS.

To conclude this analysis, it can be said that the composite electrodes, even at very low loading, outperform the bulk Pt electrodes. The increase in performance is most likely due to the efficient dispersion of Pt particles on the large surface area of the MWCNTs. In addition, the performance of the composite electrodes increases with loading for a deposition time of up to 30 minutes, which indicates that the overall catalytic activity of the electrode was due to the surface area of platinum rather than an increase in catalytic activity due to the formation of nanoparticles.

Table 1- Tafel parameters of Pt NP-MWCNT composite electrodes for various PLA times in acid electrolyte. (Presented Error is standard deviation from the mean)

PLA Time (min)	b_C **($mV.dec^{-1}$)**	**Exchange Current ($mA.cm^{-2}$)**	***j*** **at -0.09V ($mA.cm^{-2}$)**
2.5	-33±2.7	5.19±4.0	61.3±50
5	-33±0.7	6.50±0.7	79.2±40
10	-32±3.6	6.99±3.0	91.3±30
20	-80±7.3	12.2±5.0	178±4.0
30	-62±0.4	22.1±7.0	357±60
Pt wire	29.3	4.25	51.4

4.2.2 Tafel Plot in Alkaline Conditions

Figure 4.11 shows the Tafel curves for various cathodes in the hydrogen evolution region in alkaline conditions. The current density is normalized with respect to the geometric area of the electrode. Curve (a) is the response of a pure platinum wire, (b) a bare MWCNT, (c) a MWCNT with platinum deposited using PLA during 5 minutes, (d) 10 min, (e) 20 min, (f) 30 min, (g) 40 min, (h) 60 min.

Curve (a) shows that pure platinum has lower current density than the Pt NP-MWCNT composite electrodes at all overpotentials. The bare MWCNT curve (b) has the lowest catalytic activity, as it is lower by one order of magnitude or more than any Pt NP-MWCNT composite electrode.

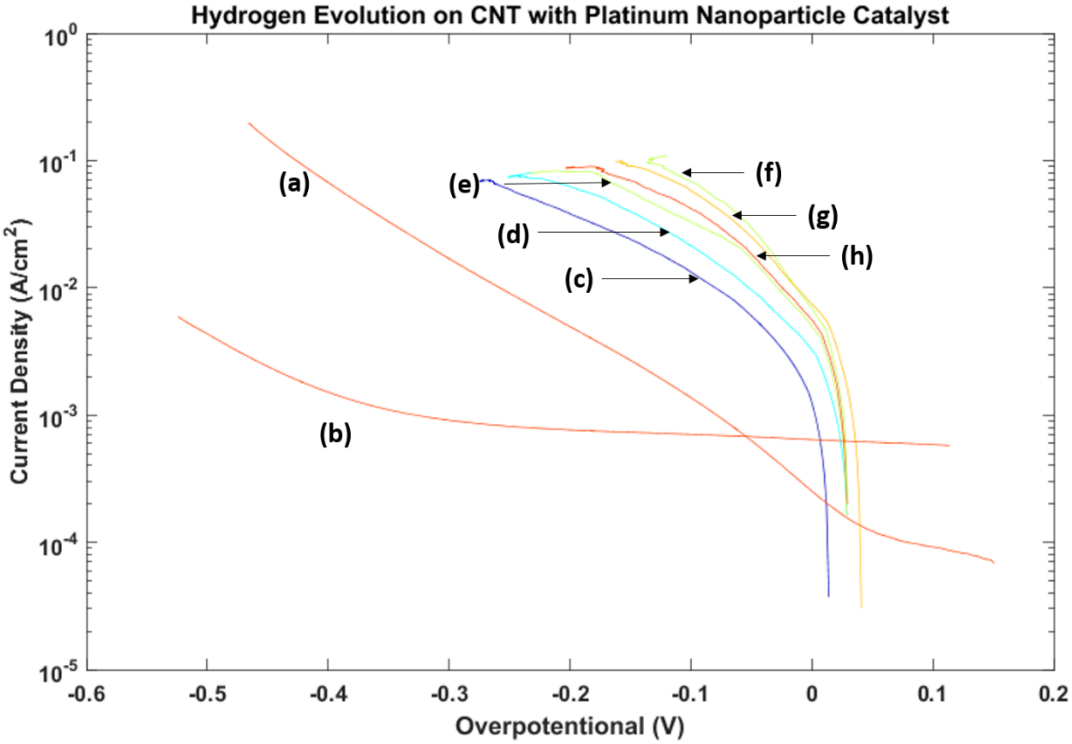

Figure 4.11-Tafel plot: Current density as a function of overpotential for various electrodes in 0.1M NaOH (a) Platinum wire, (b) Bare MWCNT, (c)2 min 30s Pt NP-MWCNT, (d) 5 min Pt NP-MWCNT, (e) 10 min Pt NP-MWCNT, (f) 20 min Pt NP-MWCNT, (g) 30 min Pt NP-MWCNT.

In order to address the variability in the current-overpotential curves and quantify the electrochemical activity of the cathodes presented in Figure 4.11, it is useful to examine the current density at a specific overpotential. This allows statistical treatment of replicated measurements done for each composite electrode. The resulting analysis is shown in Figure 4.12. This figure shows the average current density for the various Pt NP-MWCNT electrodes mentioned previously as a function of depositing time. All current densities were determined at an overpotential of -110 mV. Figure 4.12 shows that the mean electrocatalytic activity of the cathodes increases steadily with the PLA time, for deposition times of up to 30 minutes. Past that deposition time the electrode activity seems to stabilize, indicating that there is no added value in increasing the loading past this point. The fact that the electrode activity reaches a plateau indicates that the electrode surface is completely covered after a deposition time of 30 minutes. As mention in the previous section, the platinum penetrates deep into the MWCNT forest instead of forming a layer on top of the MWCNTs. Past the 30-minute deposition time it becomes useless and even wasteful in terms of money to add any platinum to the MWCNTs. Furthermore, the higher catalytic activity observed in the composite cathodes relative to the pure Pt is possibly due to the normalization with respect to the geometric area that was done for the Pt NP-MWCNT. The actual electrochemically active area of the Pt NP-MWCNT electrodes is much larger than the geometric area; therefore, there are much more catalytic sites than are being accounted for with this sample normalization.

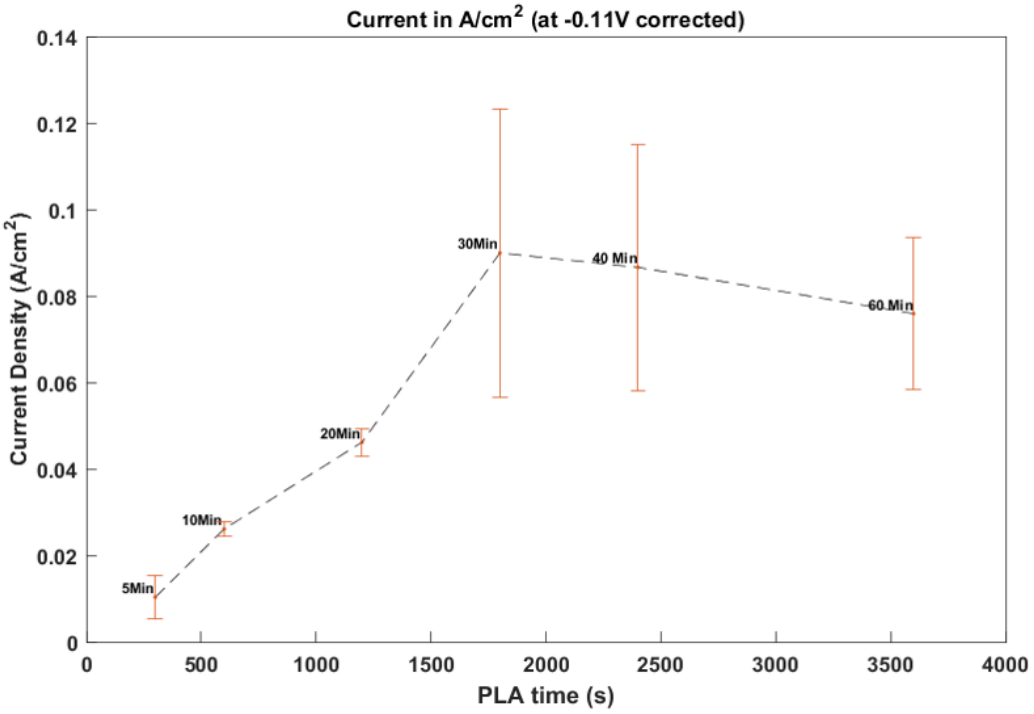

Figure 4.12- Current density normalized by unit geometric area, for various composite electrodes as a function of PLA time (measured in 0.1M NaOH)

Figure 4.12 presents the current density normalized with respect to the mass of platinum. The activity of platinum is constant at all deposition time except at 60 min. The formation of agglomerate at this high deposition time as seen in Figure 4.3-D. These agglomerate cause a large mass of platinum to be unexposed to the surface therefore a large mass of platinum is not participating in the HER.

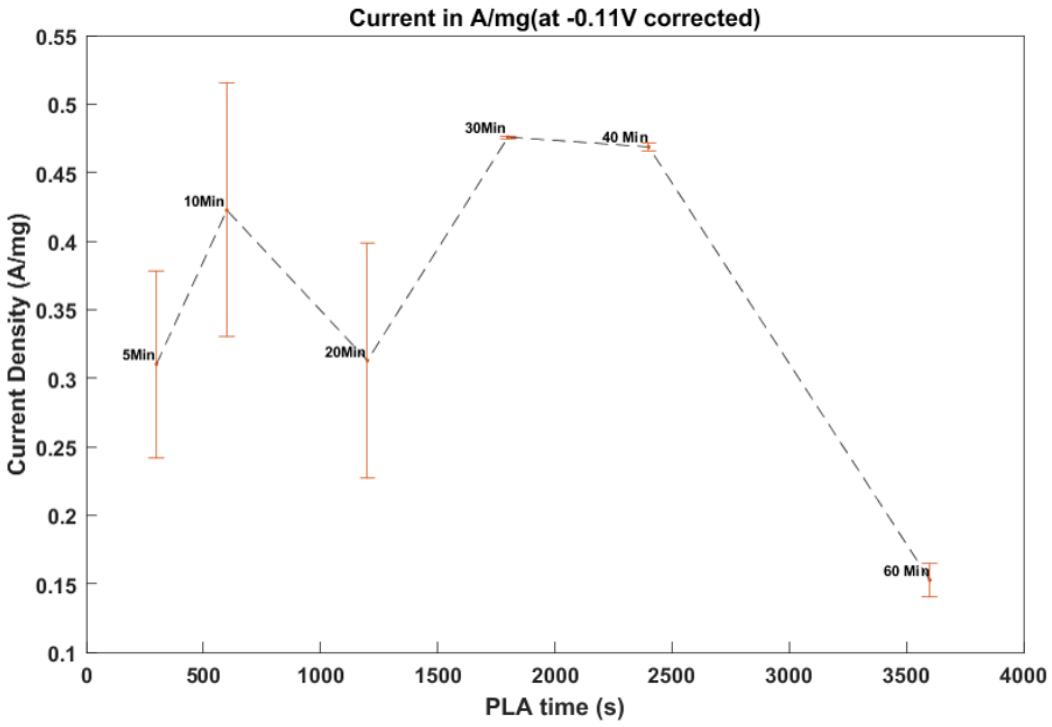

Figure 4.13- Current density normalized by mass of platinum, various composite electrodes as a function of PLA time (measured in 0.1M NaOH).

Figure 4.13 presents the same data that is presented in in Figure 4.12. However, the current density is now normalized with respect to the mass of platinum added. The current density can be assumed to stay constant despite the variability observed in replicate measurements except at 60 minutes. This indicates that activity of platinum remain unchanged with deposition time. This confirms that the increase in activity observed in the previous section is due to an increase in the MWCNT coverage by platinum, i.e. to the increase in surface area of Pt exposed to the electrolyte, and thus to the increase in surface area available to the HER. There does not seem to be any synergistic affect between MWCNTs and Pt at play. The decrese observed at 60 mins is indicative of unused mass of Pt du to agglomeration.

As before the Tafel plot provides information on the Tafel slope b_C (mV.dec^{-1}), the electron transfer coefficient α, and the exchange current density. These parameters are presented in Table 2. In addition, the current density for each composite electrode is show at the chosen potential of 110mV. The first parameter presented is the Tafel slope. It has been shown that this parameter

yields information on the limiting step in the mechanism involved in the HER. The Tafel slope observed for the composite electrodes in the alkaline solution shows great variability. However, the slopes are closest to the theoretical value of 120 mV.dec^{-1} quoted in literature for the Volmer step as the RDS [14]. Since the Volmer step is common to both possible reaction mechanisms, the complete mechanism cannot be determined using linear Tafel polarization. The large variation observed in the Tafel slope may be caused by impurities, as mentioned before, or by the heterogeneity of the electrode. Heterogeneous surfaces might lead to different RDS at various catalytic sites. The LTP method only allows us to determine an average value of the Tafel slope.

From the Tafel slopes the electron transfer coefficient α was estimated through the following relation, $\alpha=(2.3RT)/(b_C\ n\ F)$, where R is the ideal gas constant (8.314 J.mol^{-1}.K^{-1}), n is the number of electrons transferred during the HER, T is the temperature (K), and F is the Faraday constant (96485 C.mol^{-1}). This transfer coefficient is an indication of the efficiency of this reaction with respect to the anodic reaction. Therefore, a large transfer coefficient is desirable here. The electrodes have a relatively large transfer coefficient ($\alpha > 0.5$) in the region investigated.

Table 2-Tafel parameters of Pt NP-MWCNT composite electrodes for various PLA times in basic electrolyte. (Presented Error is standard deviation from the mean)

PLA Time (min)	**b_C(mV.dec^{-1})**	**α**	**Exchange Current (mA.cm^{-2})**	**j_0 at -0.11V (A.cm^{-2})**
5	-120±1.2	0.492±0.005	0.047±0.03	10.3±5
10	-83±10.4	0.713±0.089	0.85±0.3	26.1±2
20	-113±5.7	0.523±0.026	0.85±0.007	46.2±3
30	-94±0.2	0.627±0.001	1.29±0.2	89.9±30
40	-94±5.9	0.631±0.040	1.48±0.2	86.6±30
60	-87±9.0	0.686±0.072	1.88±0.7	75.9±20
Pt-wire	119	0.49	0.018	1.53

4.2.3 Electrode Stability

Figure 4.14 shows the measured potential between the working electrode and the reference electrode over time when a constant current density of 200 $mA.cm^{-2}$ is applied to a Pt NP-MWCNT electrode with a platinum deposition time of 10 minutes. The results in Figure 4.14-A were recorded over a first cycle of 24 hours. The electrolyte used (1M NaOH) was purged before the measurement started. The data in Figure 4.14-B was obtain using the same electrode used in Figure 4.14-A during a second 24-hour cycle. The two test were done consecutively. However, the electrolyte was changed after the first and purged for 40 minutes.

During the first cycle the measured potential starts out at -2.12V and decreases slowly to a more negative value of -2.3V. A more negative potential is undesirable, as it indicates that more energy would be required to maintain a steady current flow through the working electrode. At first glance this would suggest that the loss in catalytic activity may be due to the loss of platinum. During the second cycle the starting potential is -2.16V. The potential decreases rapidly to -2.3V during the first 10,000 seconds, but remains stable at that value during the remaining time. There is only a small difference between the initial potential between the two cycle. Since the initial potential in cycle two is higher than the potential at the end of cycle 1 it can be concluded that the decrease in potential observed in the first cycle is not due to an irreversible change of the electrode surface. The small difference in initial potential may be due to some fouling of the electrode due to trace impurities in the electrolyte such as calcium, nickel, or iron.

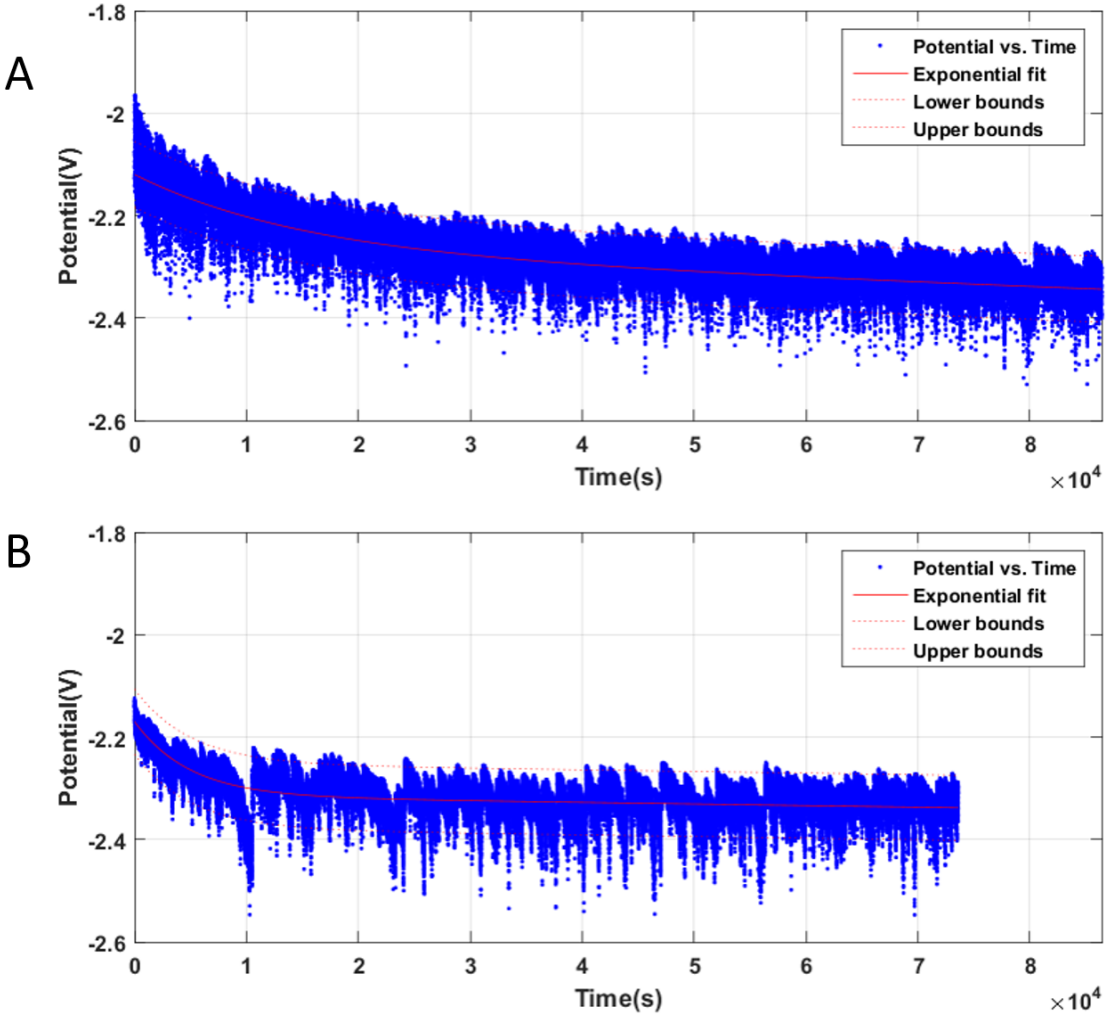

Figure 4.14-Measured potential versus time for an applied current density of 200 mA.cm^{-2} in 1M NaOH (the same electrode is used in both cycles). A) First cycle B) Second Cycle

In Figure 4.15 the average potential for both cycles is presented on the same plot. As can be seen the measured potential for both cycles converges to the same potential beyond 70,000 seconds. The fact the two cycles converge indicate that the electrode is stable. Therefore, the drop in potential observed up to 70,000 seconds cannot be attributed to a loss of Pt from the surface. The difference in trend observed at times prior to 70,000 may be due to reversible changes occurring at platinum nanoparticles. As for the initial drop in potential observed in the first 10,000 seconds may be due to blockage of the pores of the electrode by produced H_2 bubbles.

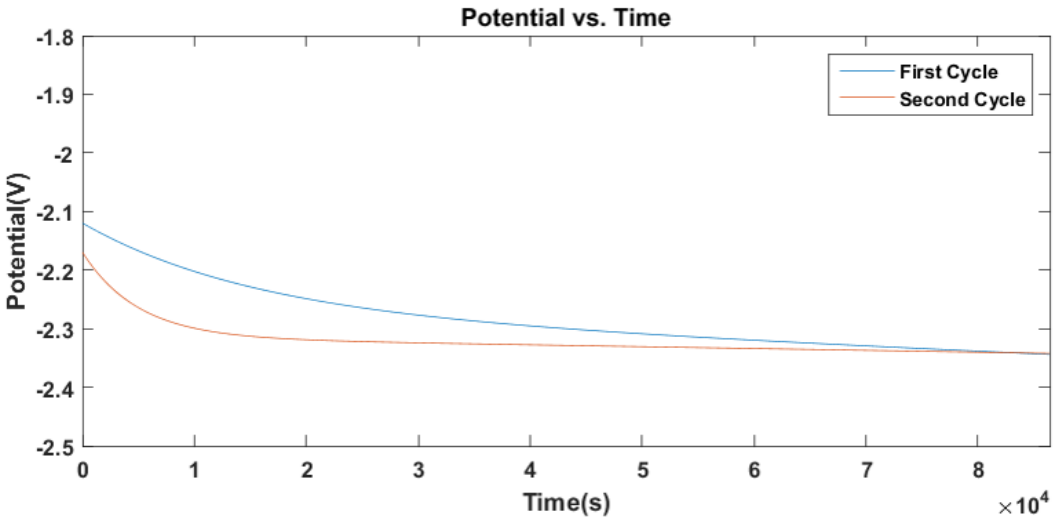

Figure 4.15-Comparison of the average measured potential versus time for an applied current density of 200 mA.cm-2 in 1M NaOH (the same electrode is used in both cycles).

4.3 Comparison of Electrode Performance with Literature

Wu et al. reported a current density of 330 mA.cm^{-2} at an overpotential of η=100 mV and temperature of 30ºC. The working electrode had a Pt and Pd loadings of 0.05 mg.cm^{-2} and 0.05 mg/cm^{-2}. The catalyst was deposited on commercial Vulcan carbon powder electrochemically [40]. The electrolyte used was 0.5M H_2SO_4. This electrode exhibits lower current density at higher overpotential than our most performant electrode (340 mA.cm^{-2} at η=90 mV with a Pt loading of 0.2 mg.cm^{-2}). Therefore, our electrode outperforms this electrode. However, this electrode has a much lower platinum and palladium loading. Our 10 min electrode with a Pt loading of 0.074 mg.cm^{-2} has the closest loading to Wu et al.'s electrode. Our 10 min electrode has a much lower current density (91 mA.cm^{-2} at η=90 mV) than Wu et al.'s electrode.

Thoi et al. reported on the performance of their catalyst for hydrogen evolution in solid acid electrochemical cells based on the proton-conducting electrolyte CsH_2PO_4. The catalyst was made using commercial CNTs decorated with Pt nanoparticles deposited electrochemically. The electrodes had a Pt loading of 0.014 mg.cm^{-2}. The reported current density was 42 mA.cm^{-2} at an overpotential of η=100 mV for a measurement temperature of 240 ºC [38]. Our lowest loading electrode (0.03 mg.cm^{-2}) showed a much higher current density of 61.3 mA.cm^{-2} than Thoi et al.'s electrode. In addition, Thoi et al. conducted their test at high temperature which is expected to speed up the kinetic of the HER. The fact that our electrode outperforms Thoi et al.'s electrode despite tis observation suggest that our electrode has superior catalytic activity.

Grigoriev et al. produced a catalyst with Pt and Pd nanoparticles deposited electrochemically on commercial Vulcan carbon powder. Typical metal loadings of 0.7 and 2.4 mg cm^{-2} were obtained for cathodes and anodes, respectively. Current-voltage curves were recorded at 90 °C during PEM water electrolysis. A cell voltage of 1.68 V yielded a current density of 1 A cm^{-2}[41].

Kiani et al. produced a platinum-coated nanoporous gold film electrode. The platinum was deposited electrochemically and formed an ultra-thin Pt coating, which behaved as the nanostructured Pt. The loading of Pt was calculated as 4.2 × 10^{-3} μg.cm^{-2}. The current density at −0.8 V vs. Ag/AgCl (η=550 mV) was 3 A.μg^{-1} of Pt. The electrolyte used was 0.1 M H_2SO_4[42]. Our electrodes exhibited current density ranging from 1 to 2 mA. μg^{-1} of Pt at η=90 mV. Despite the very high overpotential used it seems that Kiani et al,s electrode out performs our electrodes.

5 Conclusion

The ultimate objective of this work was to synthesize and characterize the performance of Pt nanoparticle decorated MWCNT based electrodes that would perform well in electrochemical energy systems. Given the high cost of platinum reducing its loading compared to commercial catalyst used for the HER was also a primordial objective in this work. The targeted application for this novel electrode is polymer electrolyte electrolyzers for the production of hydrogen from water.

In order to achieve this objective a two-step electrode fabrication process developed in the Plasma Processing Laboratory was used. The first step involved the growth of MWCNT from a stainless steel mesh using thermal chemical vapor deposition. The second step was the synthesis and deposition of the platinum nanoparticles on the MWCNT covered stainless steel mesh. The benefits of using these techniques include that very high conductivity between the stainless steel and MWCNT due to the root growth process and the high degree of control on the nanoparticle loading on MWCNTs.

Investigation of the catalytic properties of the electrodes by linear Tafel polarization revealed that our electrodes out-performed bulk platinum in both acidic and alkaline environments. The electrode performance increased with loading to a maximum activity at a loading of 0.2 $mg.cm^{-2}$. In an alkaline environment, the current density of the electrode was 89.9 $mA.cm^{-2}$ at an overpotential of 110 mV. In acidic conditions, the current density recorded was 340 $mA.cm^{-2}$ at an overpotential of 90 mV. The reduction in loading achieved in this work represents a 4 to 19 folds decrease in the amount of platinum used in the catalyst layer with respect to commercial catalysts. Given the high cost of platinum our electrodes could drastically reduce the costs of electrolyzers while simultaneously increasing their performance.

Further analysis revealed some mechanistic insight on the Pt NP-MWCNT electrode. In the alkaline, environment the Volmer step (H^+ adsorption) was determined to be the rate-determining

step. In acidic condition the Tafel step was the rate-determining step at low loading, while the Heyrovsky step at high loading.

6 References

[1] M. McArthur, L. Jorge, S. Coulombe, and S. Omanovic, "Synthesis and characterization of 3D Ni nanoparticle/carbon nanotube cathodes for hydrogen evolution in alkaline electrolyte," *Journal of Power Sources*, vol. 266, pp. 365-373, 2014.

[2] K. Krischer and E. R. Savinova, "Fundamentals of Electrocatalysis," *Handbook of Heterogeneous Catalysis*, 2008.

[3] C. E. Baddour, F. Fadlallah, D. Nasuhoglu, R. Mitra, L. Vandsburger, and J.-L. Meunier, "A simple thermal CVD method for carbon nanotube synthesis on stainless steel 304 without the addition of an external catalyst," *Carbon*, vol. 47, pp. 313-318, 2009.

[4] D. T. Whipple and P. J. Kenis, "Prospects of CO2 utilization via direct heterogeneous electrochemical reduction," *The Journal of Physical Chemistry Letters*, vol. 1, pp. 3451-3458, 2010.

[5] J. A. Turner, "A Realizable Renewable Energy Future," *Science*, vol. 285, pp. 687-689, 1999-07-30 00:00:00 1999.

[6] K. Oldham and J. Myland, *Fundamentals of electrochemical science*: Elsevier, 2012.

[7] C. G. Zoski, *Handbook of electrochemistry*: Elsevier, 2007.

[8] P. H. Rieger, *Electrochemistry*. New York: Chapman & Hall, 1994.

[9] J. O. M. Bockris and A. K. N. Reddy. (2004). *Modern electrochemistry Vol. 2B, Vol. 2B*. Available: http://site.ebrary.com/id/10067497

[10] M. Enyo, "Hydrogen electrode reaction on electrocatalytically active metals," in *Comprehensive Treatise of Electrochemistry*, ed: Springer, 1983, pp. 241-300.

[11] W. Sheng, H. A. Gasteiger, and Y. Shao-Horn, "Hydrogen oxidation and evolution reaction kinetics on platinum: acid vs alkaline electrolytes," *Journal of The Electrochemical Society*, vol. 157, pp. B1529-B1536, 2010.

[12] N. M. Markovića, S. T. Sarraf, H. A. Gasteiger, and P. N. Ross, "Hydrogen electrochemistry on platinum low-index single-crystal surfaces in alkaline solution," *J. Chem. Soc., Faraday Trans.*, vol. 92, pp. 3719-3725, 1996.

[13] B. Conway and J. M. Bockris, "Electrolytic hydrogen evolution kinetics and its relation to the electronic and adsorptive properties of the metal," *The Journal of Chemical Physics*, vol. 26, pp. 532-541, 1957.

[14] D. Pletcher, R. Greff, R. Peat, L. M. Peter, and J. Robinson, "7 - Electrocatalysis," in *Instrumental Methods in Electrochemistry*, ed: Woodhead Publishing, 2010, pp. 229-250.

[15] J. Bockris, I. Ammar, and A. Huq, "The mechanism of the hydrogen evolution reaction on platinum, silver and tungsten surfaces in acid solutions," *The Journal of Physical Chemistry*, vol. 61, pp. 879-886, 1957.

[16] S. Trasatti, "Work function, electronegativity, and electrochemical behaviour of metals: II. Potentials of zero charge and “electrochemical” work functions," *Journal of Electroanalytical Chemistry and Interfacial Electrochemistry*, vol. 33, pp. 351-378, 12// 1971.

[17] S. Trasatti, "Work function, electronegativity, and electrochemical behaviour of metals: III. Electrolytic hydrogen evolution in acid solutions," *Journal of Electroanalytical Chemistry and Interfacial Electrochemistry*, vol. 39, pp. 163-184, 9// 1972.

[18] L. Rao, N. Reddy, S. Coulombe, J.-L. Meunier, and R. Munz, "Carbon nanotubes as nanoparticles collector," *Journal of Nanoparticle Research,* vol. 9, pp. 689-695, 2007.
[19] P. Avouris, Z. Chen, and V. Perebeinos, "Carbon-based electronics," *Nat Nano,* vol. 2, pp. 605-615, 10//print 2007.
[20] A. Javey and J. Kong, "Carbon nanotube electronics," 2009.
[21] T. W. Odom, J.-L. Huang, P. Kim, and C. M. Lieber, "Structure and electronic properties of carbon nanotubes," *The Journal of Physical Chemistry B,* vol. 104, pp. 2794-2809, 2000.
[22] J. P. Metters and C. E. Banks, "Electrochemical utilisation of chemical vapour deposition grown carbon nanotubes as sensors," *Vacuum,* vol. 86, pp. 507-519, 2012.
[23] L. Hong, Y. Wen-Yan, K. Banerjee, and M. Jun-Fa, "Circuit Modeling and Performance Analysis of Multi-Walled Carbon Nanotube Interconnects," *Electron Devices, IEEE Transactions on,* vol. 55, pp. 1328-1337, 2008.
[24] A. Jorio, G. Dresselhaus, and M. S. Dresselhaus, *Carbon nanotubes: advanced topics in the synthesis, structure, properties and applications* vol. 111: Springer Science & Business Media, 2007.
[25] D. Harbec and J.-L. Meunier, "Method for producing carbon nanotubes using a DC non-transferred thermal plasma torch," ed: Google Patents, 2010.
[26] M. Kumar and Y. Ando, "Chemical vapor deposition of carbon nanotubes: a review on growth mechanism and mass production," *Journal of nanoscience and nanotechnology,* vol. 10, pp. 3739-3758, 2010.
[27] A. R. Harutyunyan, T. Tokune, and E. Mora, "Liquid as a required catalyst phase for carbon single-walled nanotube growth," *Applied Physics Letters,* vol. 87, p. 051919, 2005.
[28] S. B. Sinnott, R. Andrews, D. Qian, A. M. Rao, Z. Mao, E. C. Dickey, *et al.*, "Model of carbon nanotube growth through chemical vapor deposition," *Chemical Physics Letters,* vol. 315, pp. 25-30, 1999.
[29] R. D. Schaeffer, "Fundamentals of laser micromachining," 2012.
[30] H. Abramczyk, "1 - Basic Physics of Lasers," in *Introduction to Laser Spectroscopy,* ed Amsterdam: Elsevier Science, 2005, pp. 1-18.
[31] M. Stafe, A. Marcu, and N. Puscas, "Material Removal and Deposition by Pulsed Laser Ablation and Associated Phenomena," in *Pulsed Laser Ablation of Solids*. vol. 53, ed: Springer Berlin Heidelberg, 2014, pp. 143-214.
[32] W. T. Silfvast, *Laser fundamentals*. Cambridge; New York: Cambridge University Press, 2004.
[33] N. Hordy, S. Coulombe, and J.-L. Meunier, "Plasma Functionalization of Carbon Nanotubes for the Synthesis of Stable Aqueous Nanofluids and Poly(vinyl alcohol) Nanocomposites," *Plasma Processes and Polymers,* vol. 10, pp. 110-118, 2013.
[34] N. Hordy, N.-Y. Mendoza-Gonzalez, S. Coulombe, and J.-L. Meunier, "The effect of carbon input on the morphology and attachment of carbon nanotubes grown directly from stainless steel," *Carbon,* vol. 63, pp. 348-357, 2013.
[35] N. Hordy, D. Rabilloud, J.-L. Meunier, and S. Coulombe, "High temperature and long-term stability of carbon nanotube nanofluids for direct absorption solar thermal collectors," *Solar Energy,* vol. 105, pp. 82-90, 7// 2014.
[36] V. C. Aiping Yu, Jiujun Zhang, *Electrochemical Supercapacitors for Energy Storage and Delivery: Fundamentals and Applications*. London, GBR: CRC Press, 2013.

[37] P. Millet, F. Andolfatto, and R. Durand, "Design and performance of a solid polymer electrolyte water electrolyzer," *International Journal of Hydrogen Energy,* vol. 21, pp. 87-93, 1996.
[38] V. S. Thoi, R. E. Usiskin, and S. M. Haile, "Platinum-decorated carbon nanotubes for hydrogen oxidation and proton reduction in solid acid electrochemical cells," *Chemical Science,* vol. 6, pp. 1570-1577, 2015.
[39] C. R. Chisholm, D. A. Boysen, A. B. Papandrew, S. K. Zecevic, S. Cha, K. A. Sasaki, *et al.*, "From laboratory breakthrough to technological realization: The development path for solid acid fuel cells," *Interface*, vol. 18, pp. 53-59, 2009.
[40] M. Wu, P. K. Shen, Z. Wei, S. Song, and M. Nie, "High activity PtPd-WC/C electrocatalyst for hydrogen evolution reaction," *Journal of Power Sources,* vol. 166, pp. 310-316, 2007.
[41] S. A. Grigoriev, P. Millet, and V. N. Fateev, "Evaluation of carbon-supported Pt and Pd nanoparticles for the hydrogen evolution reaction in PEM water electrolysers," *Journal of Power Sources*, vol. 177, pp. 281-285, 3/1/ 2008.
[42] A. Kiani and S. Hatami, "Fabrication of platinum coated nanoporous gold film electrode: a nanostructured ultra low-platinum loading electrocatalyst for hydrogen evolution reaction," *International Journal of Hydrogen Energy,* vol. 35, pp. 5202-9, 06/ 2010.